AN ABSTRACT OF THE THESIS OF

Dylan D. Righi for the degree of Master of Science in Oceanography presented on February 7, 2002.

Title: Sea Surface Height and Geostrophic Velocity Variability in the California Current System as Observed from the TOPEX Altimeter.

Abstract approved: Redacted for privacy

Paul T. Strub

Eight years (1994-2000) of data from the TOPEX/Poseidon satellite altimeter are used to investigate the variability of the sea surface height and geostrophic velocity of the California Current system. The TOPEX/Posiedon satellite measures SSH along an exact-repeat set of groundtracks with a 10-day repeat cycle. In the domain studied here (140° - 110°W, 24° - 50°N) the groundtrack separation ranges from 200-300 km, decreasing with increased latitude. Along-track resolution is 5.75 km.

Variances of SSH and across-track geostrophic velocities are presented. The annual SSH and velocity variances show the envelope of high variance associated with the California Current as a C shaped region from the coast at 45°N south to an offshore limit of ~135°W between 35° - 40°N and then back toward shore south of the California Bight at 30°N. High values of velocity variance are O(400) cm^2s^{-2}

at 38°N and 126°W. Seasonal variances describe the development of the California Current system. In spring (defined here as March-May) as the system begins to develop, higher velocity variance is seen near the coast. By summer the variance has increased and moved farther offshore, before peaking in fall. Winter shows the energy moving farther offshore as it weakens. The velocity variance is partitioned into within season and seasonal mean variances to understand the contribution of inter-annual differences to the variance. The within season variance dominates in summer and fall, while the seasonal mean variance contributes significantly in winter.

The offshore transport of SSH and energy is investigated by constructing Hovmöller diagrams (time versus longitude) at different latitudes. The offshore propagation speeds are shown to compare well with theoretical Rossby wave speeds south of 35°N but to be larger by a up to factor of 1.5 north of 35°N.

The seasonal development is also described by showing seasonal wavenumber spectra on four descending and four ascending groundtracks in the domain. As the CC system develops, wavenumber energy increases at 200-300 km wavelengths on groundtracks closest to the coast. This energy propagates offshore and weakens. At the offshore tracks the wavenumbers show weaker energies and shorter wavelengths (150-200 km),

Sea Surface Height and Geostrophic Velocity Variability in the California Current System as Observed from the TOPEX Altimeter

by
Dylan D. Righi

A THESIS

submitted to

Oregon State University

in partial fulfillment of
the requirements for the
degree of

Master of Science

Completed February 7, 2002
Commencement June 2002

Master of Science thesis of Dylan D. Righi presented on February 7, 2002.

APPROVED:

Redacted for privacy

Major Professor, representing Oceanography

Redacted for privacy

Dean of the College of Oceanic and Atmospheric Sciences

Redacted for privacy

Dean of the Graduate School

I understand that my thesis will become part of the permanent collection of Oregon State University libraries. My signature below authorizes release of my thesis to any reader upon request.

Redacted for privacy

Dylan D. Righi, Author

ACKNOWLEDGEMENTS

I would like to express my appreciation for the patient and knowledgeable guidance of my advisor, Ted Strub. He has let me explore different facets of oceanography while at the same time attempting to focus my efforts towards the goal. I would also like to thank the members of my committee, Jack Barth, Bob Smith and Andreas Weisshaar, for their help in completing my degree. Irma Delson deserves my gratitude for her gentle prodding and wise counsel.

The research assistants in COAS, most notably Corrine James, Eric Beals and Priscilla Newberger have helped me immensely by sharing their experience and skills. They sometimes operate behind the scenes, but when you need it, they know where the data is buried.

Friends in Corvallis, both in and out of COAS, have made my time here enjoyable and fulfilling. Of special importance are Erik Lubbock, Kipp Shearman and Courtney Armentrout, John Lyman and Caroline Broadbent, Sue Gries, Deb Burke, Barb Lagerquist, Kate Stafford, JP Kaesermann, Tom Rippetoe, Heather Crawford, and everyone who has ever played for Disquick. I've been here long enough that this list could go on and on (even more than it did). The length of the list is indicative of how many great people I've had the luck to spend time with.

I owe my parents and family (Righis, Johnsons and Augés) much gratitude for their aid and encouragement. It is a strength to know that they will always be there for me.

Most importantly, I must express my deep appreciation to Naara. She inspires me, tortures me, makes me laugh, snuggles me, puts up with me, nourishes me, and gives me someone to come home to. Without her and her love and support I doubt I would have been able to make it through.

Which brings us to Kaila, to whom I dedicate this work. Watching her grow and discover her world is amazing and has made me realize how important it is to continue to learn and develop. The joy in her laugh is infectious and her smiles can fuel a days worth of work.

Support for this work was provided by NASA (JPL Grant 1206714) and the U.S. GLOBEC NE Pacific program (NSF grant OCE-0000900, with an additional contribution from the NASA biological oceanography program). Support for Dylan Righi was also provided by ONR grant N00014-97-1-0165.

TABLE OF CONTENTS

TABLE OF CONTENTS (Continued)

LIST OF FIGURES

LIST OF FIGURES (Continued)

SEA SURFACE HEIGHT AND GEOSTROPHIC VELOCITY VARIABILITY IN THE CALIFORNIA CURRENT SYSTEM AS OBSERVED FROM THE TOPEX ALTIMETER

1 INTRODUCTION

Strub and James [2000] describe the California Current (CC) system using data from the TOPEX, ERS-1, and Geosat satellite altimeters. Equatorward alongshore winds force the development of an equatorward jet in the spring and summer near the coast. As the jet strengthens through the fall season, it moves offshore and develops strong meanders and closed eddies. Satellite eddy kinetic energy estimates show the corresponding offshore movement of high energy and its input into the Pacific interior. Near-surface drifters deployed in the California Current system show regions of high eddy kinetic energy (EKE) near the coast which decrease offshore and to the south [*Brink et al.*, 1991; *Chereskin et al.*, 2000]. Seasonal analysis of the drifter data suggests an offshore movement of the EKE similar to the altimeter results [*Kelly et al.*, 1998]. *Swenson and Niiler* [1996] use drifter data binned into five degree bins to estimate surface velocity variability. Their results show peak variances of 200 $cm^2 s^{-1}$ at 35°N off of Pt. Conception. *Marchesiello et al.* [2001] uses a regional ocean model to show the offshore movement of surface EKE similar to that seen in satellite data.

The CC system is a large, energetic region that varies on many length and time scales. For many reasons it is important to describe this variability. Regional

fisheries are affected by when and where the onset of upwelling occurs and how the system develops into the full fledged CC system. Sea surface temperatures affect atmosphere-ocean heat exchanges and the strong gradients in the CC system play important roles. Also, the signals of the quasi-periodic El Niños are seen in the CC system: understanding exactly how the system is affected is important to being able to predict when future El Niños will occur and how they will influence the local and global climates. The results shown here are important for use in validation of computer models of the CC. Satellite data provide spatial and temporal coverage that can't be matched by ship observations.

This work extends the work of others by the use of a record length of eight years. This allows a higher confidence in the statistics of variability. Annual and seasonal variances for SSH and geostrophic cross-track velocity are presented and discussed. Wavenumber power spectra along specific groundtracks are shown to compliment the description of the seasonal development of the California Current. To investigate the interannual variability we show Hovmöller diagrams (time versus longitude) of SSH and cross-track velocity energy, and partition the seasonal variance into a within season and seasonal mean (reflective of interannual variability) components. In addition the data here covers the time period of the 1997-1998 El Niño. The effect of El Niño on the SSH and velocity variability in the California Current system will be investigated.

This work proceeds as follows: Chapter 2 describes the TOPEX altimeter and

the processing the data undergoes. Also discussed are the techniques used in constructing the various data types and figures shown. In Chapter 3 we present the analysis results. Chapter 4 presents further analysis and attempts to synthesize results shown. Chapter five contains the conclusions and highlights the important results presented.

2 DATA/METHODS

We are using eight years (1993 through 2000) of TOPEX/Poseidon (T/P) data from the NOAA/NASA Pathfinder data set. The T/P satellite covers an exact-repeat set of groundtracks with a cycle of approximately 10 days. The along-track resolution of the data set is 5.75 km and the horizontal distance between crossovers is 270 km at 30°N, decreasing as latitude increases. Poseidon is an experimental sensor and collects only 5% of the data. For this analysis we use only TOPEX data.

A satellite altimeter measures the distance between the satellite and the ocean surface. To extract the portion of this signal due to ocean currents, a number of errors must be removed, one of the larger being the uncertainty in the exact shape of the marine geoid (the shape the ocean surface would have in the absence of any movement in the ocean). Since the marine geoid is time-invariant, it's contribution to the sea surface height signal can be removed by subtracting the temporal mean of the entire dataset from each cycle. This also removes the portion of the signal due to the mean ocean flow, leaving a data set of sea level anomalies (SLAs). Some studies attempt to replace the mean SSH by adding in a climatological mean dynamic height field (i.e., *Levitus and Gelfeld* [1992]), but since here we are interested in the annual and seasonal variation of SSH and velocity, we do not take this approach. Other major error sources inherent in satellite altimetry include ocean tides, orbit error, path delays due to the wet and dry atmosphere,

the ionosphere, effects due to surface waves and electromagnetic bias, and the inverse-barometer effect (the response of the SSH to atmospheric pressure loading) [*Chelton et al.*, 2001].

In order to remove data outliers we carry out additional quality control filtering on the time series at each groundtrack point. The mean and standard deviation of the time series are computed with each point removed, and a smoothed time series is constructed using a running mean over 7 points. Then all points which are three standard deviations away from the mean (the standard deviation and mean computed without that data point) and two standard deviations away from the smoothed time series are removed. In a second step, the mean and standard deviation of the new time series are calculated and all points that are five standard deviations away from the mean are removed.

Many of our analyses are performed directly on the along-track data, while other analyses use gridded fields. In all gridding, we use the method of successive corrections [*Bratseth*, 1986]. This method estimates values at grid points by making an initial guess based on a weighted mean of surrounding data points, and then decreases the spatial scale of the quadratic weighting function. The isotropic scales used here are 2.0°, 1.25°, and 1.0°. For snapshots in time, all data within 15 days of the requested date are included in the calculations. Data are weighted in time with an exponential function:

$$W_t = exp(-\frac{1}{1.44\,T^2}(t_{obs} - t_{gr})^2)$$

where t_{obs} and t_{gr} are the data times and the grid date, and T is the 15 day weighting factor. The factor 1.44 is chosen such that data at the edge of the 15 day window is weighted half as important as data in the center of the window.

For the seasonal and intra-seasonal variances, the gridded data are binned depending on their date. Winter is defined as the months of December, January and February, with the rest of the seasons following. Seasonal variances are calculated as the variance around the annual mean (which should be zero since we have removed the 8-year mean from each data point). "Intra"-seasonal variances are calculated as the variance with the seasonal means removed.

2.1 SSH means and variances

2.1.1 Along-track SSH means and variances

The total SSH variance (referred to as the "annual SSH variance") is computed at each ground-track point by removing the long-term temporal mean for the complete 1993-2000 period. For most points in the region we have data from 286 cycles. Using data from the seasons as defined above, seasonal means of the SSH SLA are calculated. "Seasonal SSH variances" are calculated by removing the long-term mean from SSH SLA data for each season. We have also calculated "intra-seasonal variances" by removing the seasonal means from SSH SLA data for each season. These are nearly identical to the seasonal variances and are not shown here.

No effort is taken to remove seasonal steric height variations in the along-track SSH SLA data. This seasonal steric height signal is caused by the annual cycle of heating and cooling and shows up as consistently negative values in offshore locations in spring (end of the cooling cycle) and positive values in fall. These variations contribute to the seasonal SSH variances in the offshore regions.

2.1.2 Gridded SSH means and variances

Gridded sea surface height anomaly maps are created at ~15 day intervals over the 8 years from 1993 to 2000 using the successive corrections method, as described above. The grid covers the region from 110° to 140°W and 24° to 50°N with grid point spacing of 0.5° latitude by 0.5° longitude. Although the T/P ground tracks do not resolve features at 0.5° scale well, use of this grid spacing allows better resolution of onshore-offshore gradients near the tracks. As for the along-track data, the temporal mean of SSH at each point over the entire analysis period (1993 - 2000) is removed before any calculation.

In order to minimize the effect of the seasonal steric height signal on SSH variations, the mean SSH from all data that fall within the 30-day space/time window is subtracted from each point before gridding. This mean is calculated from data points along all groundtracks in the region bounded by the grid edges (110° - 140°W , 24° - 50°N) and within 15 days of the central time.

From these 15 day gridded SSH data, the annual SSH variance at each grid

point is calculated. Variances are normalized by $n-1$, where n is the number of data at each grid point (200). Seasonal means and variances are calculated as for the along-track data, removing the long-term mean in the calculation of seasonal variances.

2.2 SSH Hovmöller diagrams

To construct Hovmöller diagrams TOPEX SSH data must be binned as a function of time and offshore distance. We calculate the Hovmöller diagrams for latitude bands. All TOPEX groundtrack points that fall within a requested latitude band and 1500 km of the coast are binned as a function of distance to the closest coast point in that band. The altimeter data at these points that occur at times falling within 15 days of the center time are included in the binning. The data in each bin are averaged and the result is smoothed in the offshore direction using a loess smoother [*Schlax and Chelton*, 1992] with a half-span of 60 km. The binning is calculated every fifteen days, resulting in 200 data times over the 8 year period. Since 30 days of data are used, each 15 day interpolation is not independent from the preceding and following interpolation. We are essentially smoothing over three 10-day repeats.

Before every 15 day binning and averaging, the mean of all the SSH data that falls within the defined latitude band and 30 day time window is removed to reduce steric height signals. This is different from the mean removal method used when

gridding the fifteen day SSH maps, in that the mean removed is over only the defined latitude swath instead of the entire domain.

2.3 Cross-track velocity

To calculate cross-track geostrophic velocity anomalies at each location on a ground-track, we use centered along-track height differences separated by 5 along-track points in each direction (for TOPEX $\sim 5.75 \times 10 = 57.5$km). The resulting velocities are smoothed in the along-track direction using a loess filter with a half-span of 50 km. Because the loess smoother does not perform well near data edges, we use instead a running mean near groundtrack ends and missing data gaps larger than 25 km. All further references to velocities are to these geostrophic cross-track velocities.

2.3.1 Cross-track velocity variances

Cross-track velocity variances are calculated along the groundtracks. All data are used for the annual variance. The seasonal variances are calculated by removing the long-term (8 years, 286 cycles) mean. Seasons are defined as before, winter is December-February, etc.

2.3.2 Gridded velocity variances

Gridded maps of cross-track velocity variance are calculated from the variances at each groundtrack point, using the same grid as for the SSH variances. The map of

annual velocity variance is constructed from the annual cross-track velocity variances (above), using all data from 1993 - 2000 (286 cycles). The seasonal variances are gridded from the seasonal cross-track velocity variances (again above).

This is different than the process used to construct gridded SSH means and variances. There, the scalar along-track SSH data are gridded every fifteen days; then means and variances are found from the gridded fields. Since we have only one component (cross-track) of the vector velocities, we first form the variances at each along-track point, then grid these variances using the same succesive corrections procedure as used for SSH.

2.4 'pseudo'-EKE Hovmöller diagrams

We refer to the cross-track velocity variances as 'pseudo'-EKE to remind us that we are using only one component of velocity: the velocity in the cross-track direction. The pEKE Hovmöller diagrams are constructed in the same manner as the SSH Hovmöller diagrams, except that we begin with the square of the cross-track velocity at groundtrack points. Data are binned as a function of distance to the nearest coast point and averaged at fifteen day intervals.

2.5 Partitioning of the seasonal velocity variance

Although the calculation of seasonal means is straightforward, the calculation of seasonal variances is less so, in the sense that one has the choice of removing

either the overall temporal mean or the mean of each season. Above, we define the "seasonal variances" as those formed by removing the overall mean:

$$\sigma^2_{\text{seasonal}} = \frac{1}{N_s - 1} \sum_{i=1}^{k} \sum_{j=1}^{n_{si}} (x_{sij} - \bar{x})^2$$

where $\bar{x}$ is the mean over the entire record, x_{sij} are the n_{si} data in each season (s) and year (i), over k years. The "intraseasonal variances" as those formed by removing the seasonal mean:

$$\sigma^2_{\text{intra}} = \frac{1}{N_s - 1} \sum_{i=1}^{k} \sum_{j=1}^{n_{si}} (x_{sij} - \bar{x}^s)^2$$

Here, $\bar{x}^s$ refers to the mean of data in all years in a certain season. Both the seasonal and intraseasonal variances are normalized by $N_s - 1$, where N_s is the total number of observations that fall within each season, considering all years together.

The intraseasonal variance can further partitioned into two parts:

$$\sum_{i=1}^{k} \sum_{j=1}^{n_{si}} (x_{sij} - \bar{x}^s)^2 = \sum_{i=1}^{k} \sum_{j=1}^{n_{si}} (x_{sij} - \bar{x}^{s_i})^2 + \sum_{i=1}^{k} \sum_{j=1}^{n_{si}} (\bar{x}^{s_i} - \bar{x}^s)^2$$

where $\bar{x}^{s_i}$ is the mean of the data in a season of a particular year. The first term on the right-hand side of the equation represents the "within season variance", or the variance around the mean of each individual season in each year, summing over all years. For TOPEX, these means are based on approximately 9 cycles for each individual season. The last term describes the "seasonal mean variance", which is the variance contributed by interannual differences in the individual seasonal

means. Note that the above relation only holds true for the sums of squares, not the mean squares or variances. To construct the actual within season variance, the sum of squares is normalized by $N_s - k$, where N_s is again the number of observations (approximately 72 over the 8 years) and k is the number of years (8). The seasonal mean variance is normalized by $k - 1$.

The seasonal variance can be partitioned in a similar manner:

$$\sum_{i=1}^{k}\sum_{j=1}^{n_{si}}(x_{sij} - \bar{x})^2 = \sum_{i=1}^{k}\sum_{j=1}^{n_{si}}(x_{sij} - \bar{x}^s)^2 + N_s(\bar{x}^s - \bar{x})$$

The first term on the right-hand represents the already defined intraseasonal variance. The second contributes variability due to differences between the seasonal mean and the longterm mean. This term will later be shown to be negligible when we look at the across-track geostrophic velocity variances.

2.6 Wavenumber spectra along tracks

The wavenumber spectra of cross-track geostrophic velocity along selected groundtracks are calculated. The power spectral density of each groundtrack cycle is computed and then averaged over seasonal time periods. This is done for the four descending TOPEX groundtracks closest to the North American coast (descending tracks go from the west to east in the northern hemisphere). Track separation is approximately 200 km. Only groundtrack points in the latitude band between 25° and 45°N are used. We also calculate the wavenumber spectra for the four ascending TOPEX tracks that intersect the coast between 35° and 45°N. The

southern-most groundtrack clips the northern edge of Monterrey Bay, the second intersects the coast at Point Arena, the third between Cape Blanco and Cape Mendicino, and the northern-most in central Oregon. Points north of 25°N are used on these ascending tracks.

3 RESULTS

3.1 Seasonal variation

3.1.1 SSH

The annual SSH variance plotted along T/P groundtracks is shown in Figure 3.1. The envelope of variance due to the California Current system covers a C-shaped region from the coast at 45°N south to an offshore limit of ~135°W between 35° - 40°N and then back toward shore south of the California Bight at 30°N. Higher variances in what are usually considered the quiescent offshore regions (west of 130°W) are due in part to the inclusion of the seasonal steric height signal.

Due to the removal of the spatial mean in each 30 day period while constructing the gridded fields of SSH anomaly, the gridded map of annual SSH variance (Figure 3.2) does not reflect the influence of the steric height variance. This causes the C-shaped area of high variance to stand out stronger against the background of the quieter offshore domain. The high variance envelope has maximum values on the order of 100 cm^2 which are found in the middle of the "C" at 38°N and from 129°W - 125°W . Also, the energetic signature of a strong offshore eddy during the later part of 1998 can be seen in both Figures 3.1 and 3.2 at 49°N , 135°W [*Crawford et al.*, 2001].

The along-track seasonal means of SSH are shown in Figure 3.3. For both ascending and descending tracks, positive values of SSH are represented by sticks

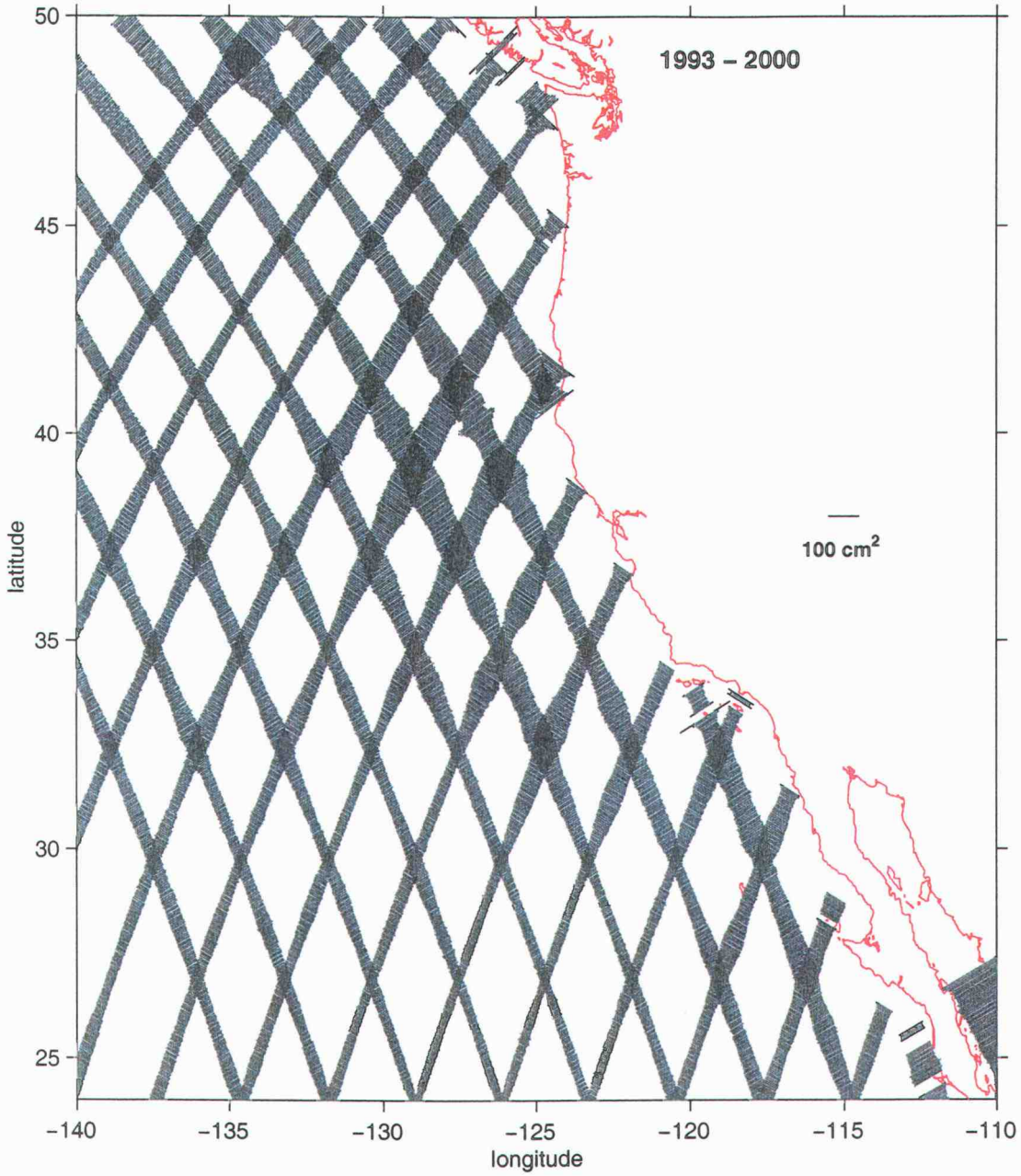

Figure 3.1: Sea-surface height variance from 1993 - 2000 along TOPEX ground-tracks.

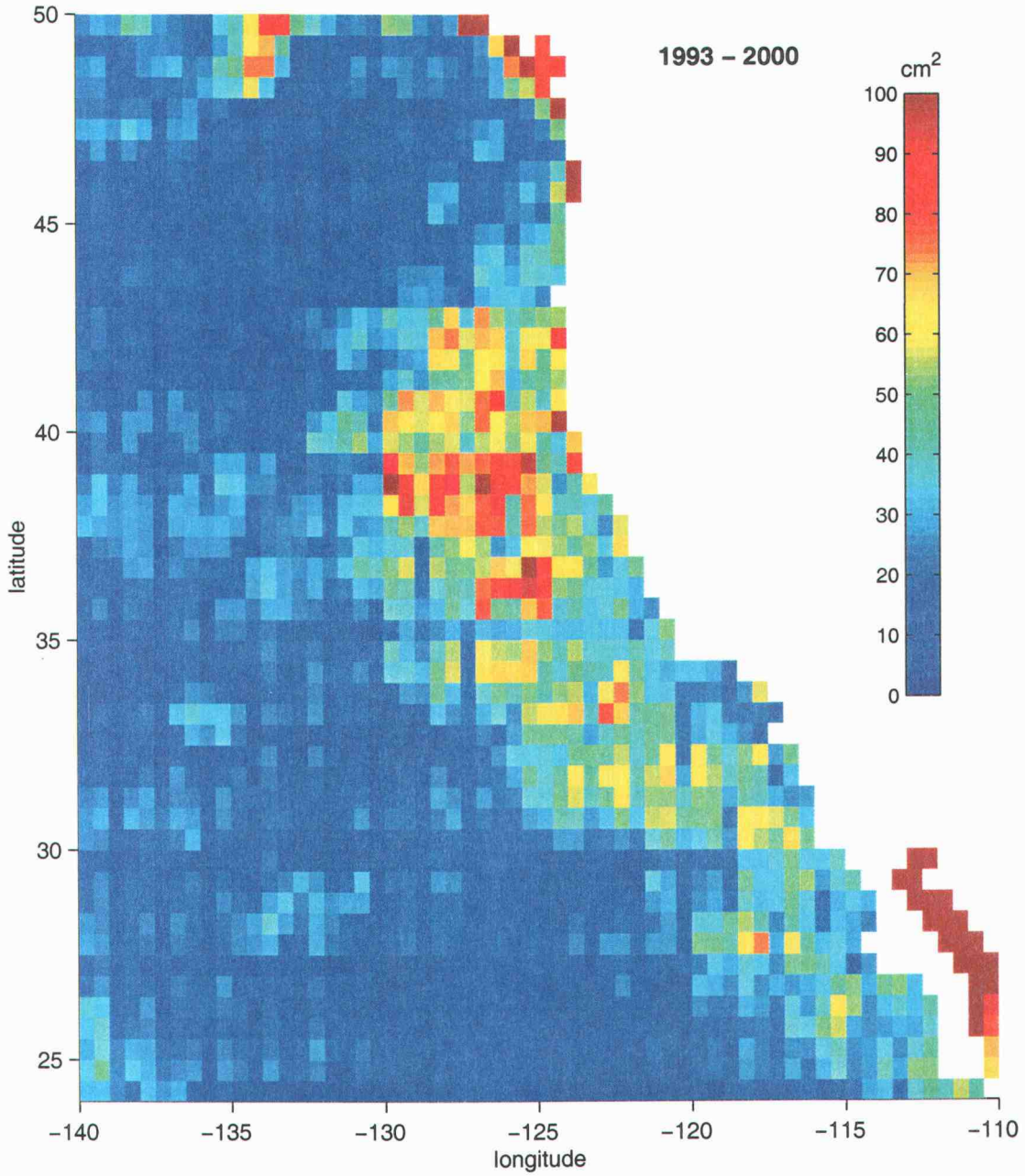

Figure 3.2: Gridded sea-surface height variance from 1993 - 2000.

on the north side of each groundtrack (i.e., the majority of the offshore values in fall are positive). Since no attempt was made to remove the seasonal steric height variation, it dominates the signal in most of the domain. This is seen in the offshore lowering of SSH at the end of the cooling season in spring, and the generally high SSH in fall after summer heating.

To discuss the seasonal signal of SSH means due to the development of the California Current system in Figure 3.3, we must look at SSHs relative to the background steric height changes. As with the height variance, the seasonal development and offshore movement of high (winter) and low (summer) bands of SSH anomaly are more clearly defined in the gridded seasonal SSH fields (Figure 3.4) due to the decreased influence of the steric height signal. In winter, high SSHs are seen near the coast north of 34°N consistent with the northward flowing Davidson current. These relative highs are still evident in spring but have moved further offshore. Near coast values south of 45°N show low SSHs developing, marking the beginning of the upwelling season. By summer the region of high SSH values have moved farther offshore and the region of low SSH next to the coast has widened north of 34°N corresponding to the fully developed upwelling season. The fall map shows this lower SSH region expanding offshore and along the coast. Finally, returning to winter, the low signal has separated from the coast.

The along-track seasonal SSH variances (Figure 3.5) are also affected by the steric height signal since they are defined as variance around the long term SSH

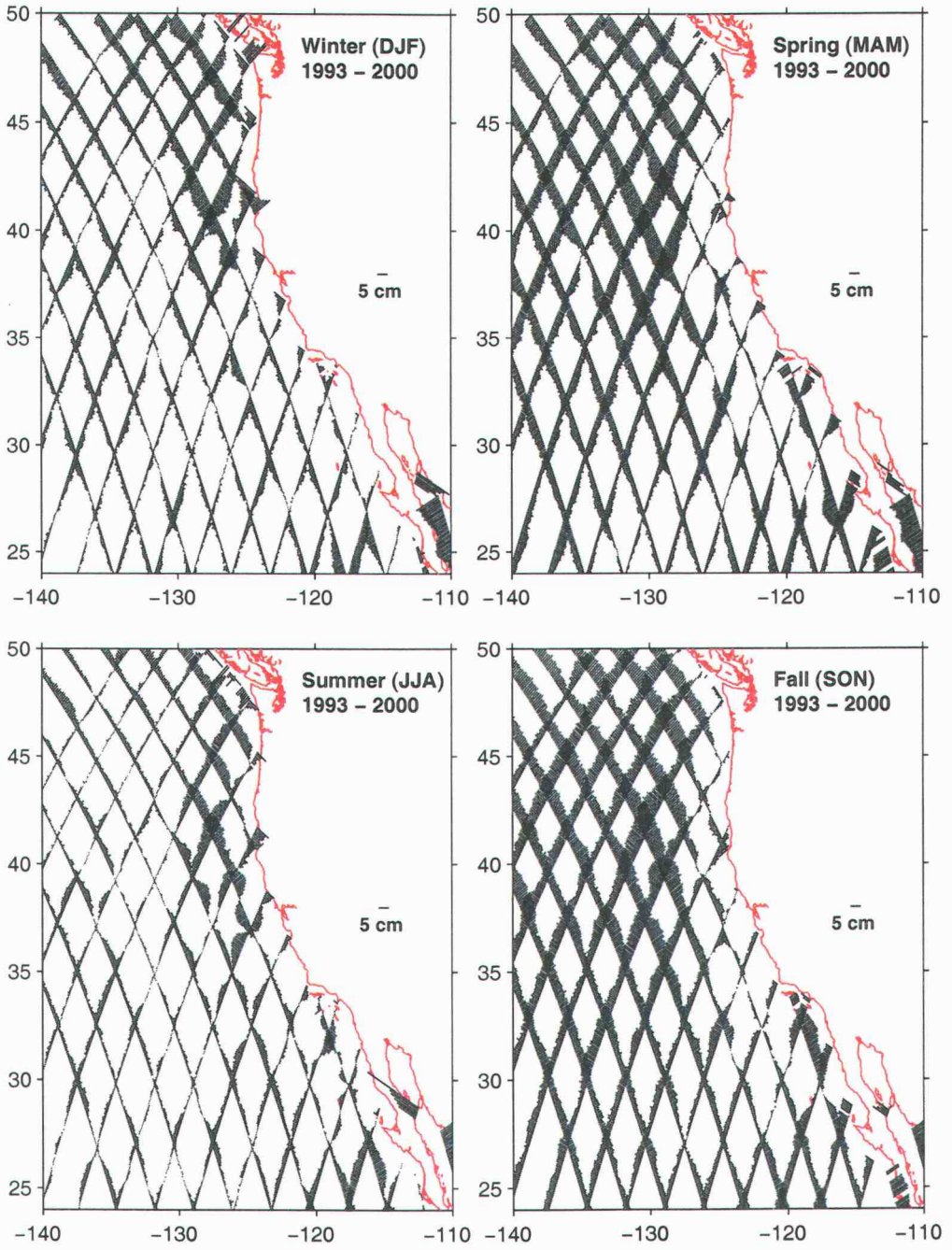

Figure 3.3: Seasonal sea-surface height means from 1993-2000 along TOPEX groundtracks. Positive values are represented by sticks on the northern side of both ascending and descending tracks.

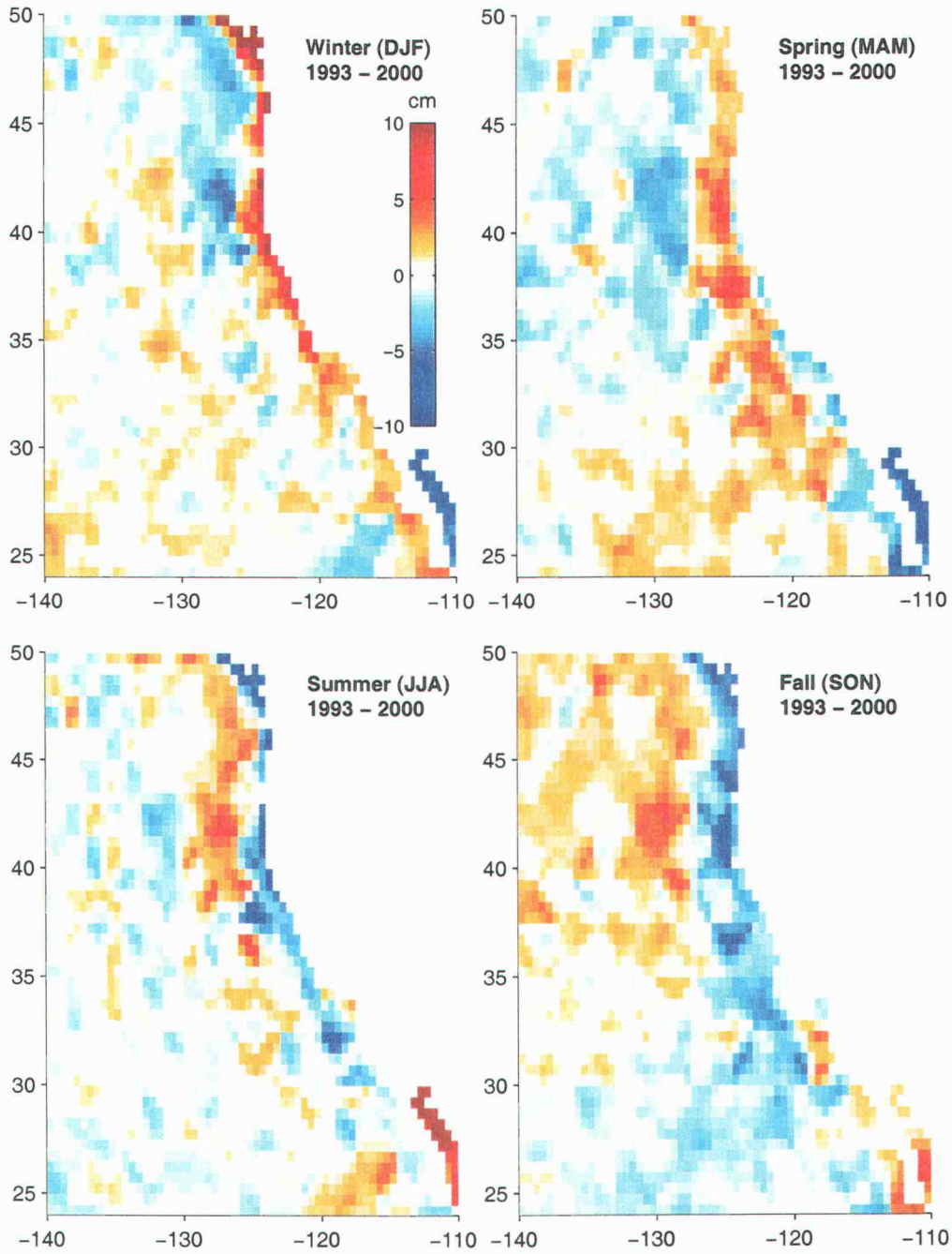

Figure 3.4: Gridded seasonal sea-surface height means from 1993-2000.

mean (zero by definition since we are working with SLAs). Thus the steric height changes contribute to the larger offshore values of SSH variance during spring and fall when the SSH is significantly lower and higher (respectively) than zero. Looking at the gridded seasonal SSH variances presented in Figure 3.6, the offshore variances are more consistently low over all seasons. The energetic California Current system can be seen clearest in summer with higher variance offshore in the band within ~5° of the coast, maximum 150-300 km from the coast. In fall the variance strengthens and moves farther off-shore and in winter and spring it dissipates. The eddy offshore at 49°N , 135°W previously discussed shows up in the summer, fall and winter SSH variances and can be seen to be moving to the south-west over those seasons. This eddy was formed during the winter of 1997-98 and moved into the area in the summer 1998 [*Crawford et al.*, 2001]. It shows strong eddies in individual years can influence the variance statistics, especially in this relatively quiet region.

3.1.2 Crosstrack Velocity

Since the velocity results are not affected by the seasonal steric height signal (the steric SSH changes over large space and time scales and thus does not contribute strongly to gradients used in the calculation of geostrophic velocity) the seasonal development of the California Current system is clearer in the velocity variance results.

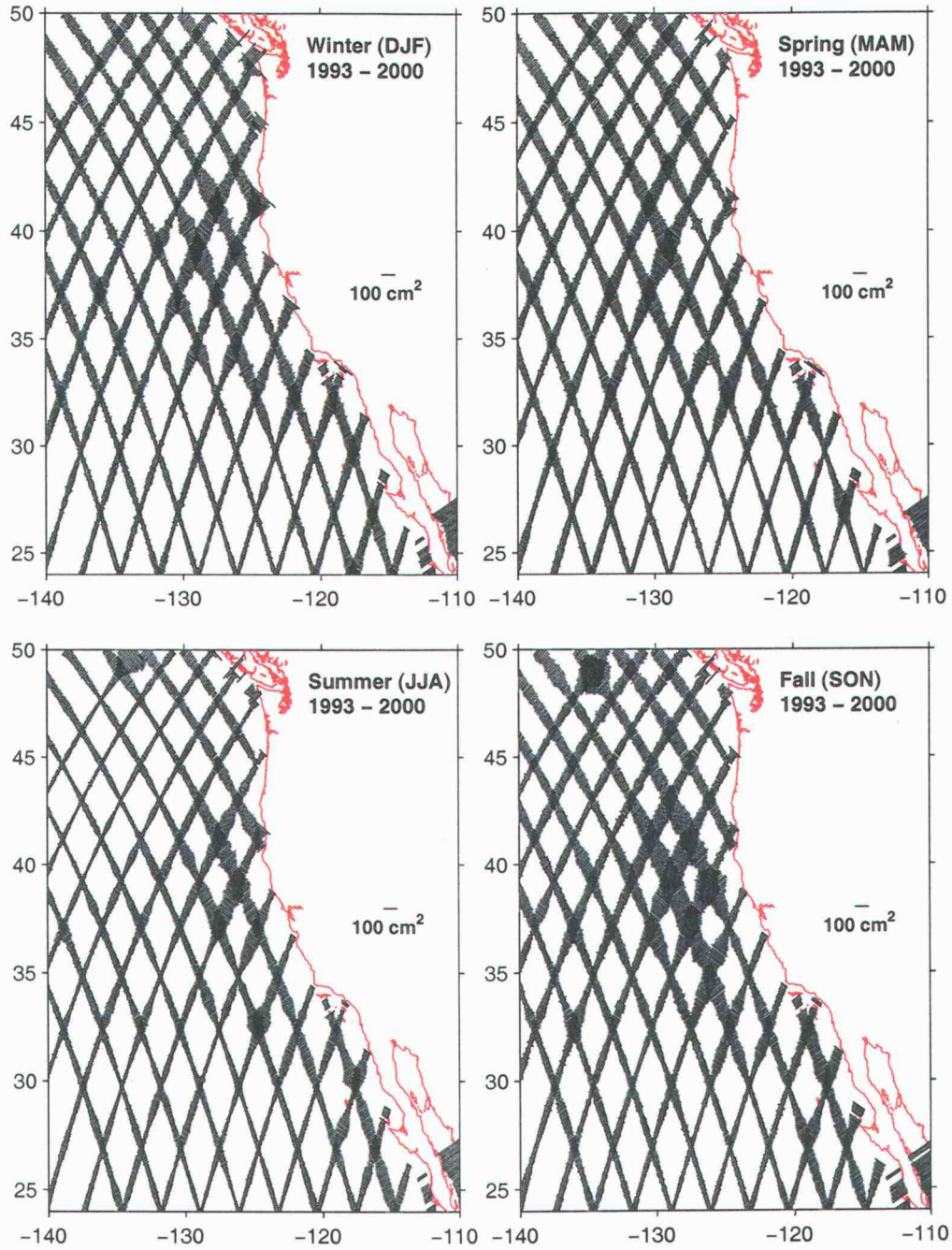

Figure 3.5: Seasonal sea-surface height variance from 1993-2000 along TOPEX groundtracks.

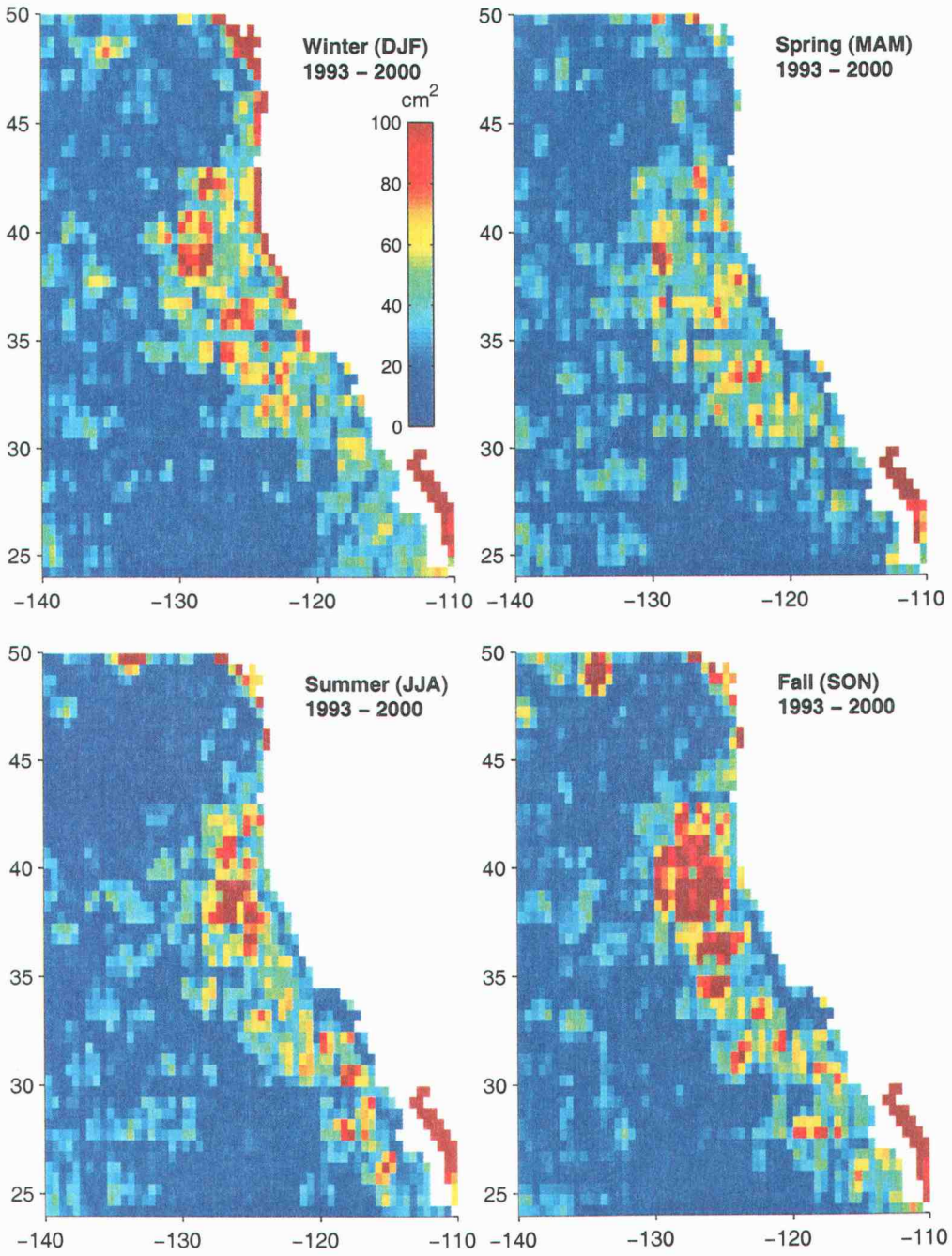

Figure 3.6: Gridded seasonal sea-surface height variance from 1993-2000

The annual variance for cross-track geostrophic velocity seen in Figures 3.7 and 3.8 shows the region of high variance due to the California Current in the "C" shaped region described in the SSH results. The maximum velocity variance is $\sim$400 cm^2s^{-2} at 38°N and 126°W . The far offshore (west of 130°W) and northern parts of the domain show the expected low energies of this part of the ocean.

The seasonal velocity variances (Figures 3.9 and 3.10) show the development of the CC system more clearly than the SSH variances (Figures 3.5 and 3.6). Equatorward currents begin to develop in spring near the coast as indicated by the high variances around 38°N , where Figure 3.4 shows low SSH associated with equatorward flow. The SSH field in Figure 3.4 indicates the jet has moved offshore in summer, while Figure 3.10 shows a strong increase in energy. There are high values south of Cape Blanco in a region within 500 km of the coast, maximum $\sim$300 km from the coast. In fall the energetic region has expanded and has spread westward. The winter plot shows decreased but still significant variance values as the CC surface jet weakens in the offshore region. The signal of the 1998 offshore eddy can be seen again in Figure 3.9 in the summer and fall velocity variances at 49°N, 135°W . Not as obvious in the SSH variance, but strongly evident here, is the energetic region in the southern part of the California Bight and along Baja California near the coast in summer.

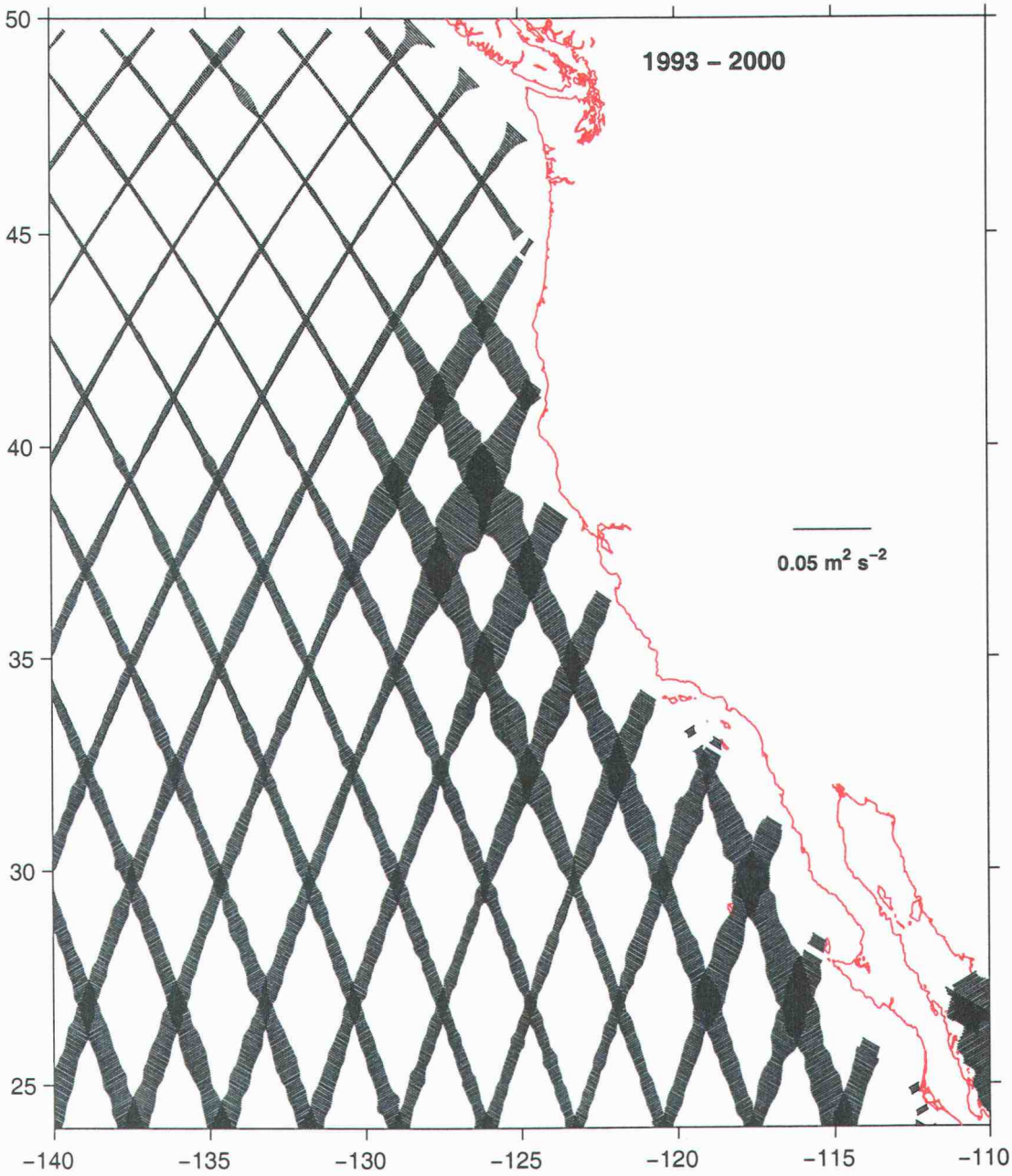

Figure 3.7: Geostrophic velocity variance from 1993 - 2000 along TOPEX ground-tracks.

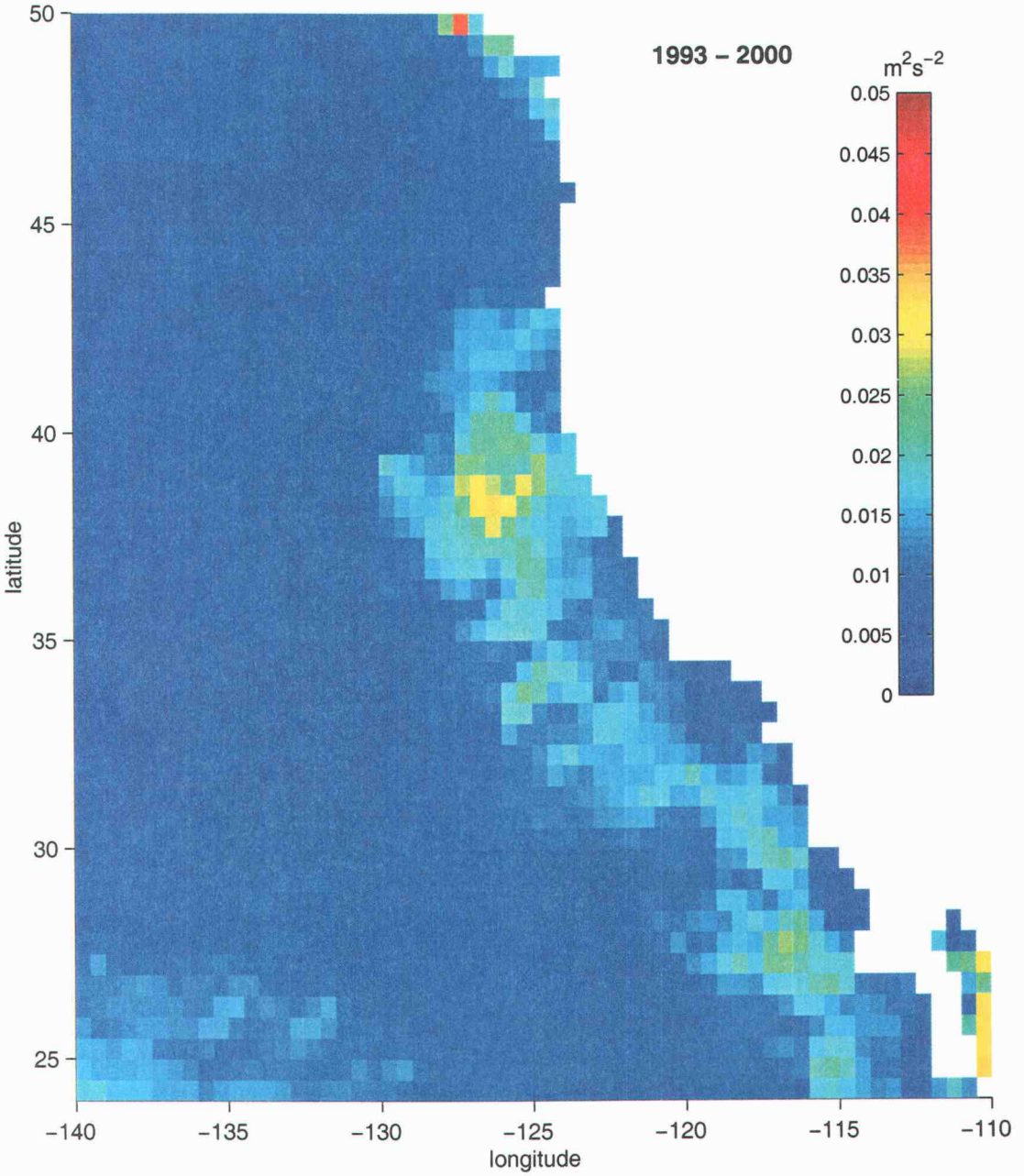

Figure 3.8: Gridded geostrophic velocity variance from 1993 - 2000.

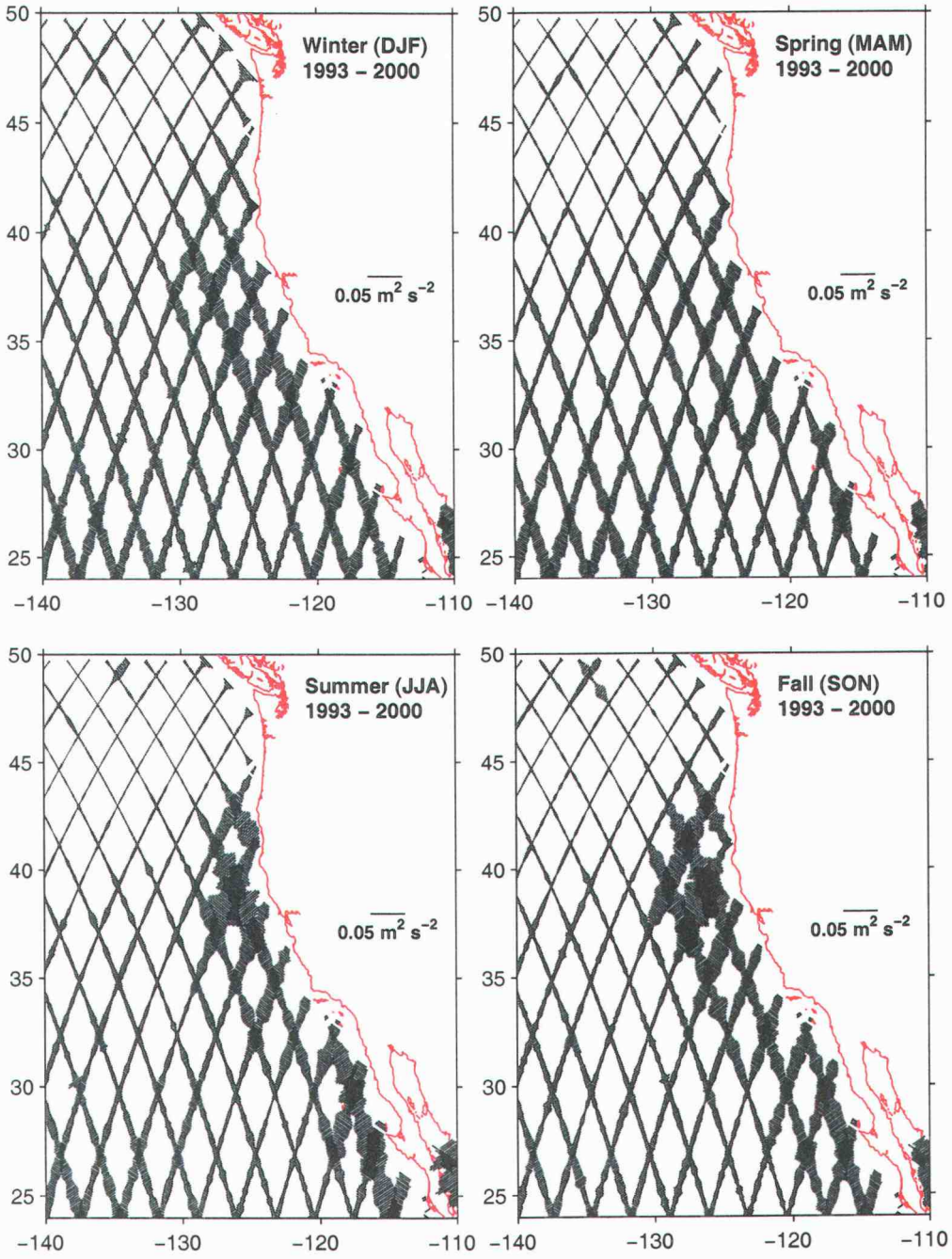

Figure 3.9: Seasonal geostrophic velocity variance from 1993-2000 along TOPEX groundtracks.

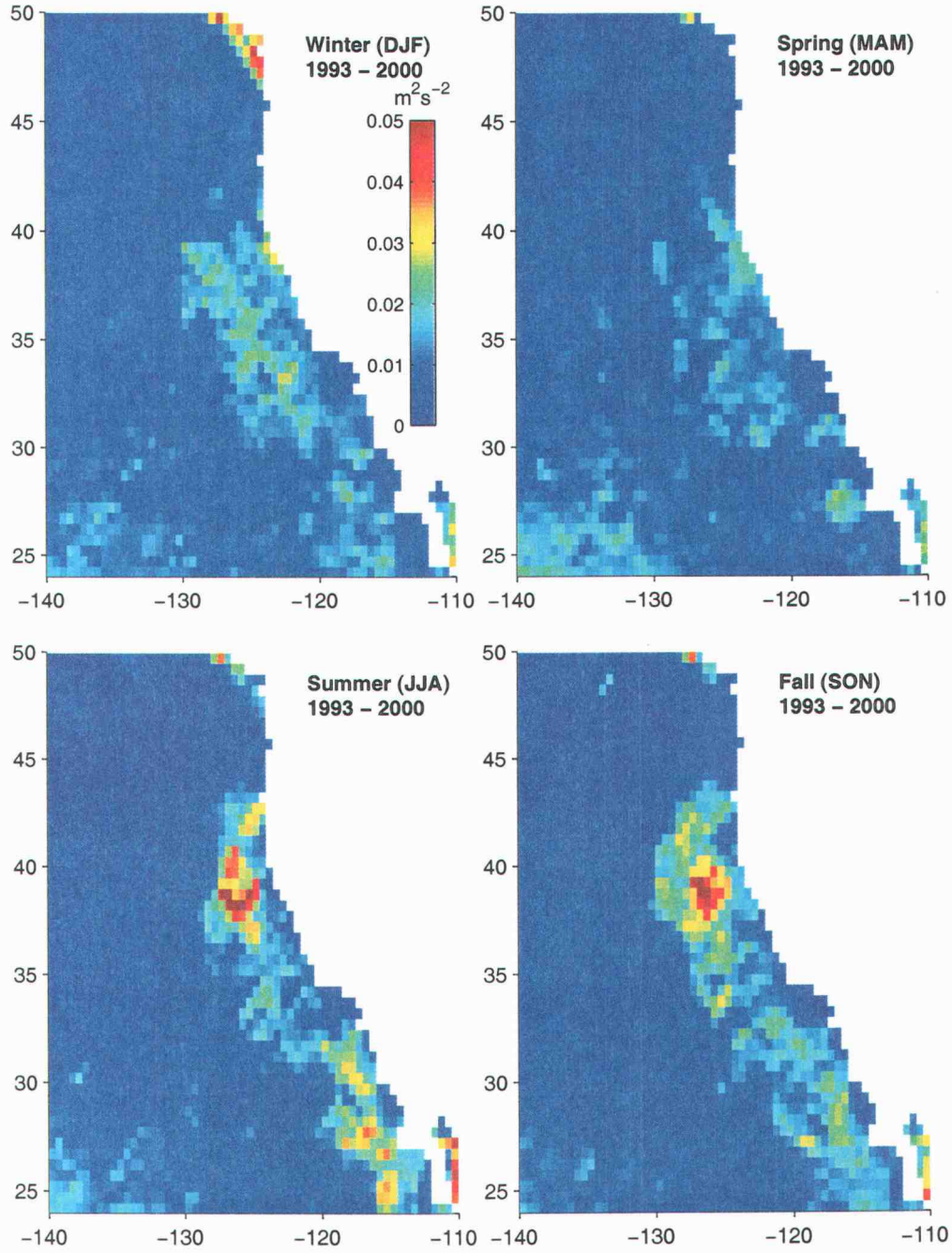

Figure 3.10: Gridded seasonal geostrophic velocity variance from 1993-2000.

3.2 Inter-seasonal variation

3.2.1 Hovmöller diagrams

The Hovmöller diagram for the SSH in the latitude band 35°N - 41°N is shown in Figure 3.11. This latitude band covers the California coast from Point Conception to Cape Mendicino where the seasonal signal in SSH and velocity is strongest. The left panel shows the variation of SSH over the eight years 1993 - 2000 as a function of offshore distance (kilometers). The alternating highs and lows of the seasonal upwelling signal develop close to the coast and propagate far offshore. In most years, the transition at the coast from high to low SSH occurs in the May-June period. The strongest feature is the signature of the 1997-98 El Niño: a high SSH anomaly develops near the end of 1997 and early 1998 and propagates offshore. The subsequent low corresponding to upwelling following the El Niño winter development is not as well defined in summer 1998 as in some previous years. On the other hand, the winter highs in 1999 and 2000 are also weak and there appears to be an overall drop in SSH following the El Niño.

The lower right panel shows the 8-year mean Hovmöller diagram, repeated three times. (The aspect ratio of the two Hovmöller panels is the same so the offshore propagation can be compared.) In the yearly mean, the low SSH begins to develop near the coast in June and reaches its minimum in late September. The nearshore highs begin in December and reach their maximum in February. Offshore (~600-800 km) it seems the high SSH anomaly is able to persist longer

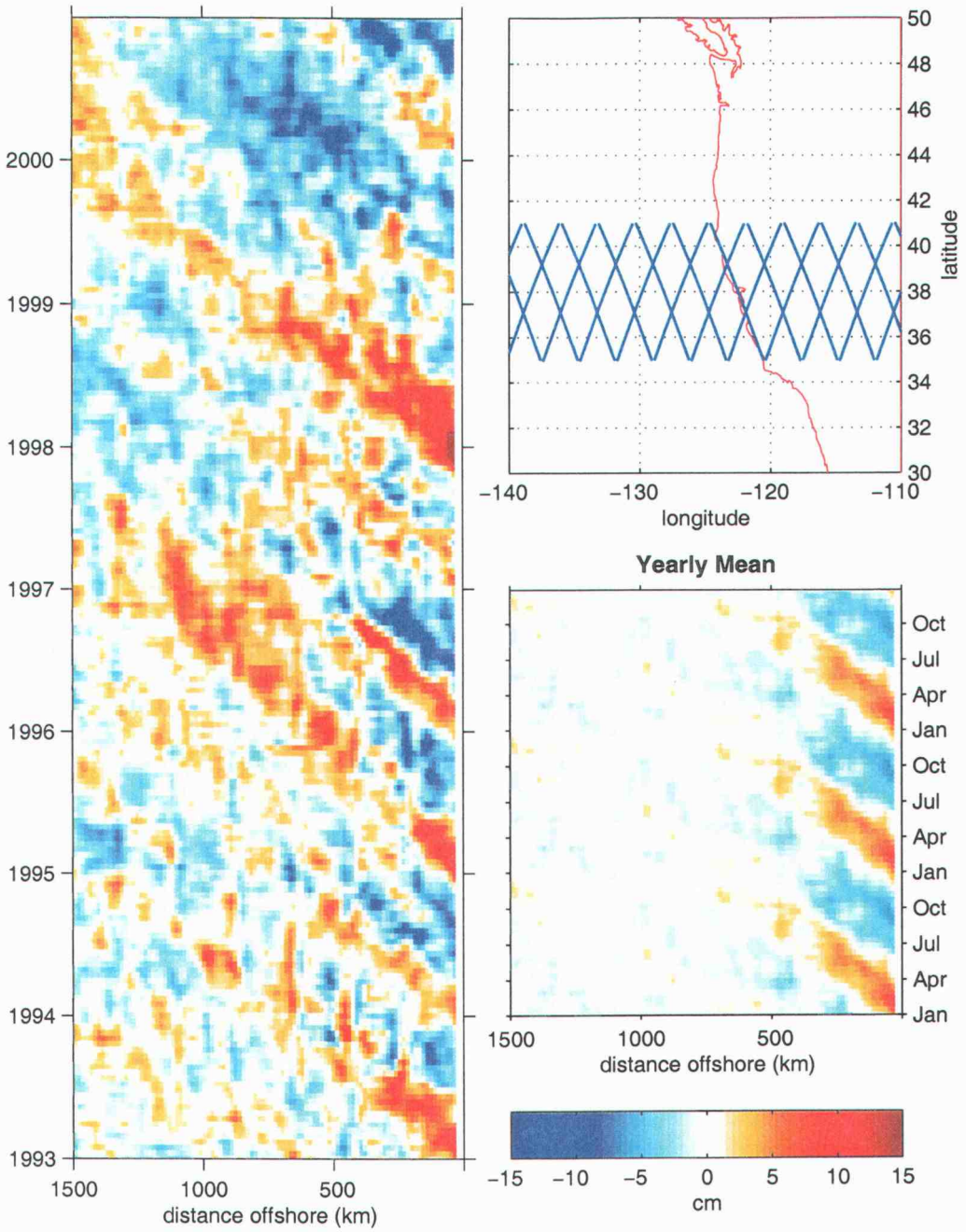

Figure 3.11: Hovmöller diagram for TOPEX SSH anomaly in the latitude band 35°N - 41°N . The left panel shows the time variation for 1993 - 2000 and the lower right shows the yearly mean annual cycle, repeated three times. The upper right panel shows the TOPEX groundtracks used.

than the low anomaly, but looking at the full Hovmöller diagram, this is probably controlled by strong signals during 1995 and the 1997-98 El Niño signal.

The Hovmöller diagram for a higher latitude band shows similar results. Figure 3.12 presents the Hovmöller diagram for 41°N - 48°N . The main differences are that the offshore propagation of SSH signals is not as strong. In addition the speed of propagation is slower, as might be expected from planetary wave theory.

The Hovmöller diagrams for what we have termed "psuedo EKE" (pEKE) are shown in Figures 3.13 and 3.14. It is "psuedo" because only the square of the cross-track component of velocity anomaly at each groundtrack point is included. In the latitude band 35°N - 41°N (Figure 3.13) the signal in the summers of 1993-1996 are similar: coherent high pEKE developing in April-May and propagating offshore to 500-600 km. In the summer of 1997 the energetic signal begins at the same time but is less coherent as it moves offshore. In 1998 the velocities are suppressed and what pEKE there is develops later. The signal continues to be less coherent in 1999 than in 1993-96. The development in 2000 looks more like the 1993-1996 pattern.

Farther north in the band 41°N - 48°N (Figure 3.14) the pEKE values are much lower and reach maximum values later in the year. Also they do not progress as far into the offshore region. The full record and the yearly mean show the offshore propagation speed to be slower than in the southern latitude band.

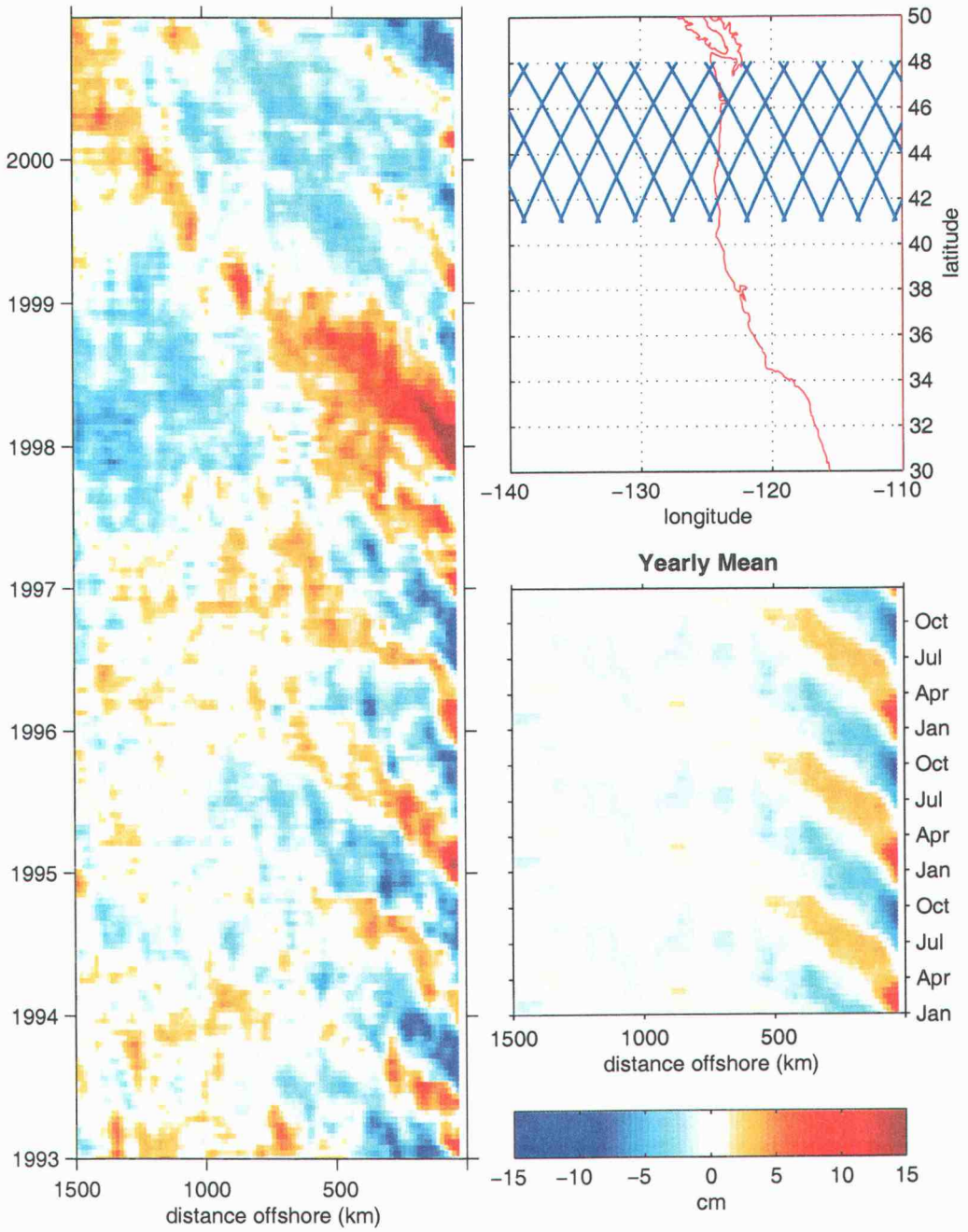

Figure 3.12: Same as for Figure 3.11, but for the latitude band 41°N - 48°N .

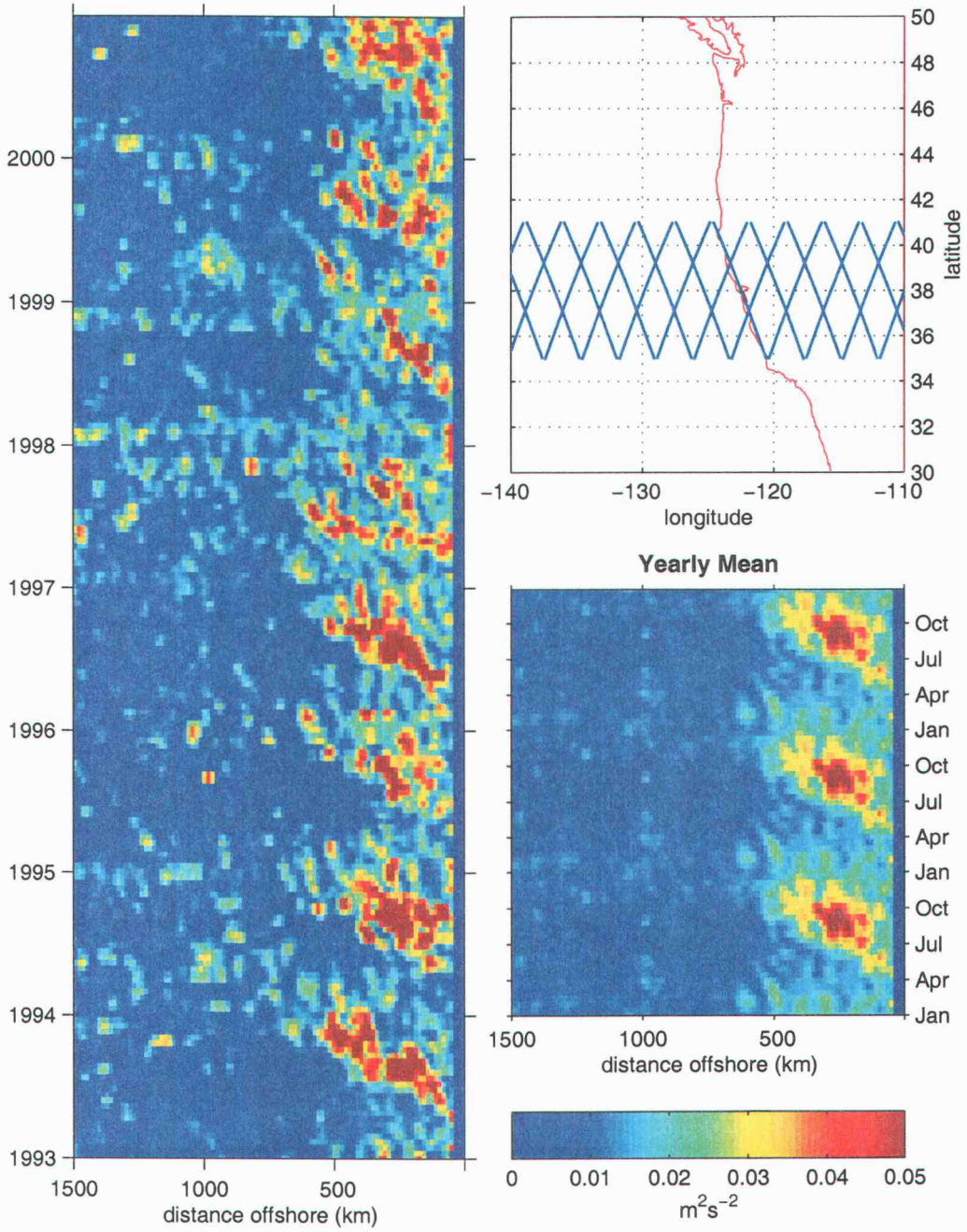

Figure 3.13: Hovmöller diagram for the square of across-track velocity from TOPEX groundtracks in the latitude band 35°N - 41°N .

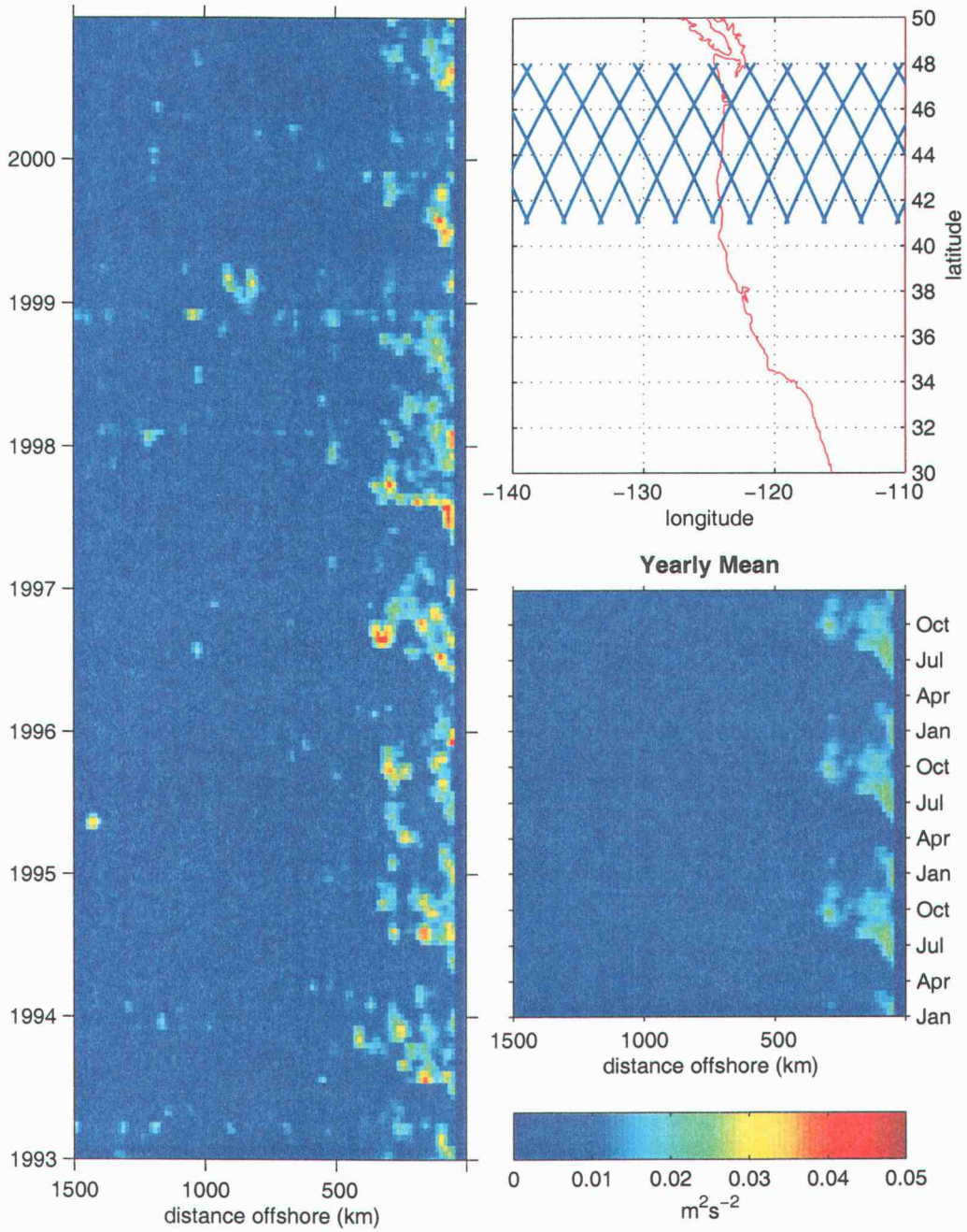

Figure 3.14: Hovmöller diagram for the square of across-track velocity from TOPEX groundtracks in the latitude band 41°N - 48°N .

3.2.2 Along-track intra, within season and seasonal variances

The variance of geostrophic velocity around 8-year seasonal means (the "intraseasonal variance" as defined in Section 2.5) is shown in Figure 3.15. These plots are very similar to the simple seasonal variances (around the long-term mean, Figure 3.9). Differences are hard to pick out. As discussed in Section 2.5 the seasonal and intraseasonal variances differ by the addition of $N_s(\bar{x}^s - \bar{x})$. The seasonal velocity means (not shown) were found to be small and the longterm geostrophic velocity anomaly mean is zero by definition. Thus the extra term contributes little to the difference between seasonal and intraseasonal variances.

The intra-seasonal variance is equal to the sum of the within seasonal variance (shown in Figure 3.16) and the seasonal mean variance (shown in Figure 3.17) before normalization. The within season variance in Figure 3.16 has similar spatial patterns to the intraseasonal variance (Figure 3.15), but the magnitudes show differences. In winter, the within season variance is significantly smaller. Spring also shows lower variance magnitudes with higher values being constrained to within $\sim$300 km of the coast. The summer within season variances show the closest seasonal match with the intraseasonal variance. The fall magnitudes are again smaller, especially south of 35°N in the California Bight and off Baja. Also, the signature in the within season variance of the 1998 eddy in the northern part of the domain is reduced in all seasons compared to the intraseasonal. This difference is strongest in fall where the variance is smaller by a factor of two.

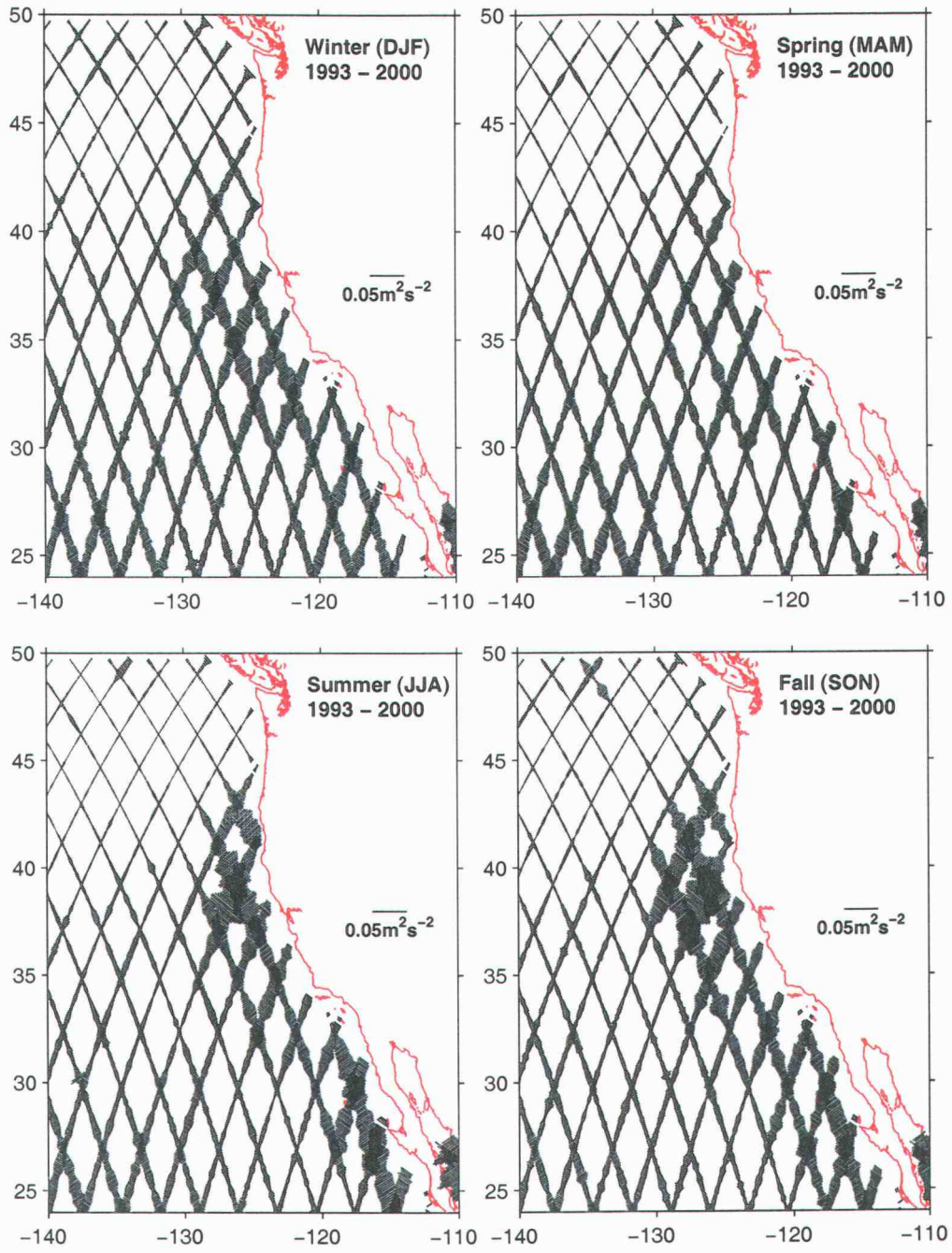

Figure 3.15: Intra-seasonal geostrophic velocity variance from 1993-2000 along TOPEX groundtracks. Intra-seasonal variance is the defined as the variance around seasonal means calculated over 8 years.

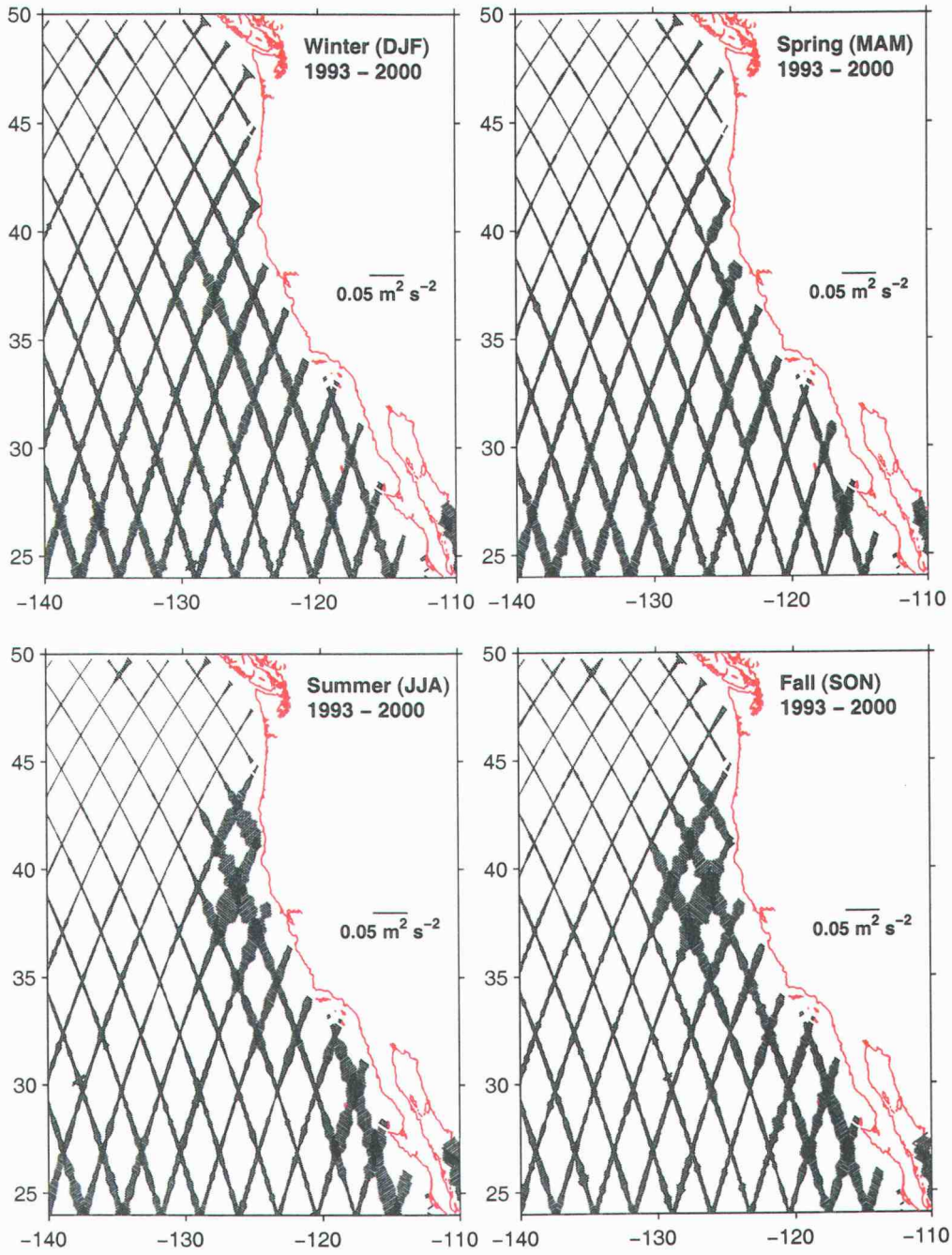

Figure 3.16: Within seasonal geostrophic velocity variance from 1993-2000 along TOPEX groundtracks. Within seasonal variance is the defined as the variance around each individual seasonal mean (over three months).

The seasonal mean variance of geostrophic velocity is a measure of how the mean of each yearly season differs from the 8 year mean of that season. Figure 3.17 shows the seasonal mean variance normalized by $k-1$. (This figure is plotted at half the scale as the other normalized along-track velocity variances, but it should be noted that direct comparisons of magnitude between figures isn't applicable since here the length of the cross-track sticks represents the amount of variance per 90-day season. In the other figures normalized length represents the variance per 10-day cycle.) In winter the seasonal mean variance describes the high variance "C" discussed earlier, with scattered energy peaks in the offshore regions. Spring values in the C region are reduced and spread out. The summer brings about localization of the energetic C region again, and the magnitudes increase in fall. Offhsore in the summer there are non-localized highs which have dissipated by fall.

Lastly, the variance due to the 1998 northern eddy shows up here in all seasons. It is strongest in fall and can be tracked moving to the south west through winter and spring. In summer it shows up both as it starts through the domain in 1998 (the elevated variance on the ascending track at 134°W) and as it reaches the edge of the domain the following summer (on both ascending and descending tracks at 47°N and 138°W).

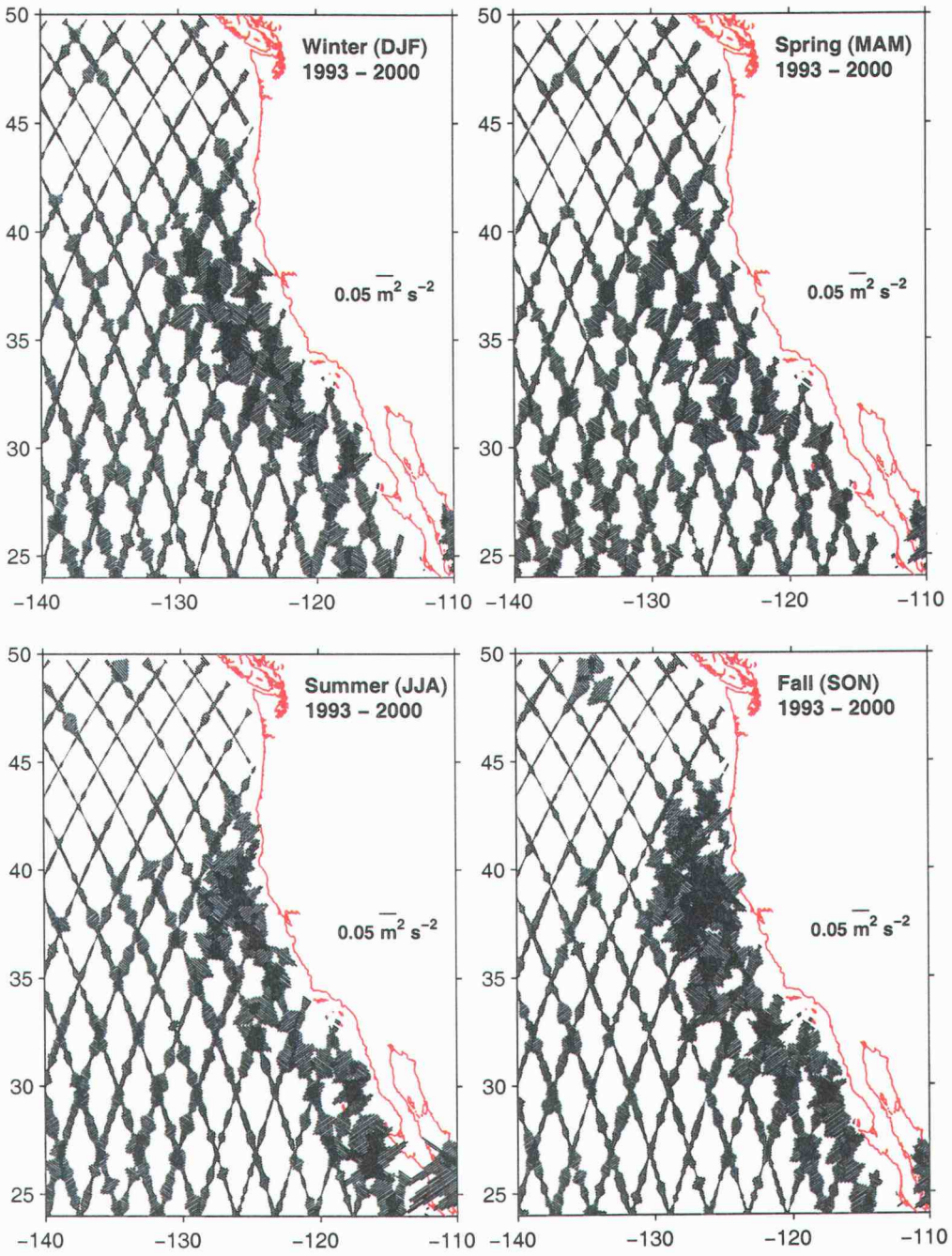

Figure 3.17: Variance of the seasonal geostrophic velocity means from 1993-2000 along TOPEX groundtracks.

3.2.3 Wavenumber spectra variation

Figure 3.18 shows the seasonal wavenumber spectra for across-track geostrophic velocities on the four descending tracks paralleling the coast between 30° and 50° N (refer to Figure 3.1 for track locations). Offshore separation of these tracks is approximately 200 km.

Spring (Mar/Apr/May) is the least energetic season. The three inshore lines show peaks energies at wavelengths from 200-300 km and the farthest offshore line has a peak at ~160 km. Summer and the development of the California Current brings higher energies to the inshore line with a high of approximately 100 cm^2s^{-2} at a 220 km wavelength. The groundtrack 400 km from the coast (blue dash-dot line) also shows higher energies, but at a slightly longer wavelength.

In fall the nearshore line energy reaches its maximum values. The 400 km offshore track has also increased and shows a broader peak centered at a 300 km wavelength. This reflects the development of the California Current as it increases in strength and moves offshore. The farthest offshore groundtracks do not show an energy increase in fall suggesting that the quiescent offshore domain is not yet influenced by the CC variability. The winter panel shows the energy at the nearshore groundtrack decreases from fall, while the second offshore groundtrack reaches its maximum. The 600 and 800 km offshore lines also have increased values, suggesting that the offshore movement of the CC energies is finally influencing the far offshore domain.

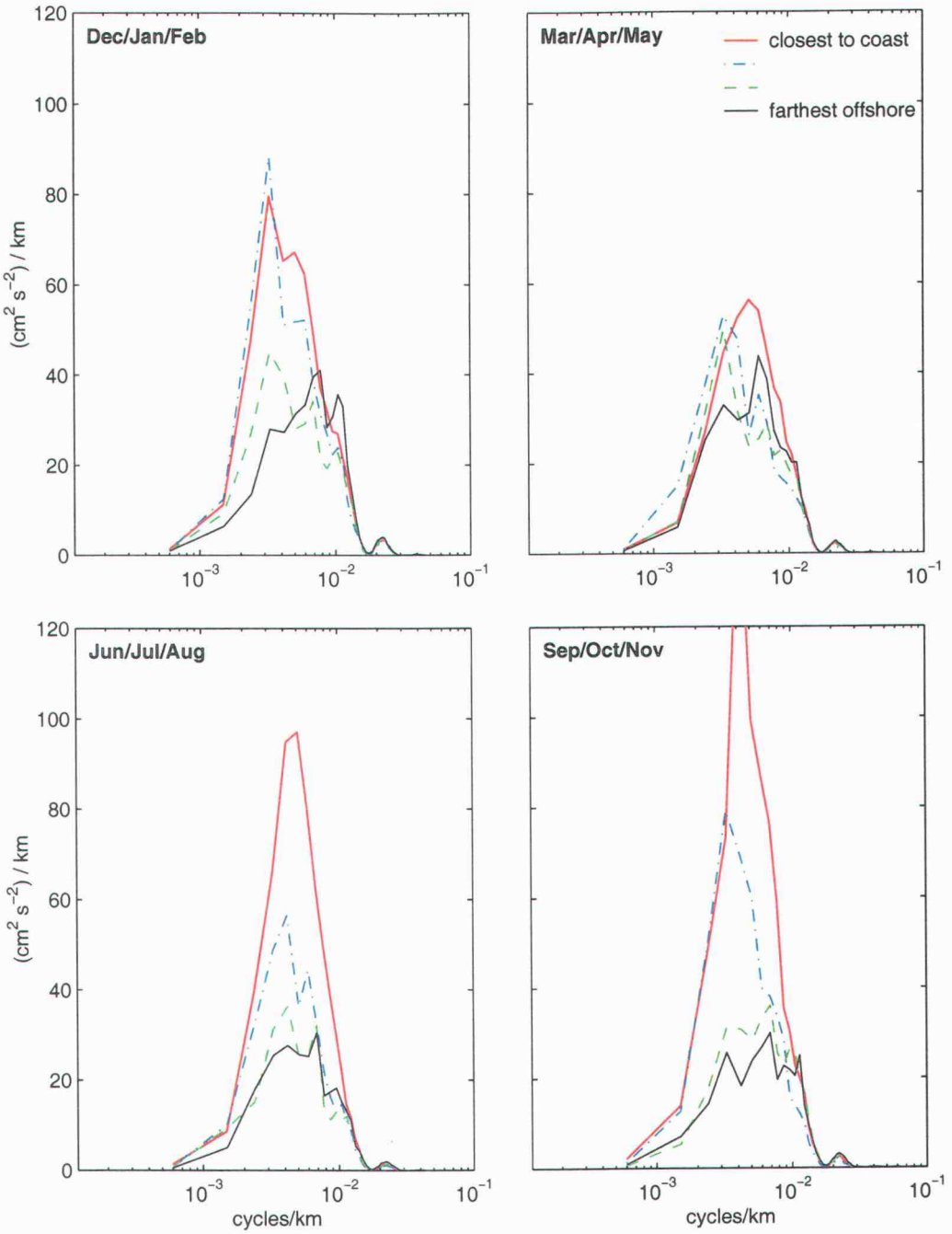

Figure 3.18: Wavenumber spectra from 1993 - 2000 for across-track geostrophic velocities on the four descending tracks closest to the coast. Groundtrack points between 30° and 50°N are used.

We can get another view of the development by looking at the seasonal wavenumbers on the ascending tracks. Figure 3.19 presents the wavenumber spectra along the four tracks that intersect the coast between 35° and 45°N. The geostrophic velocities from 1993-2000 are binned in two month bins and averaged to present a seasonal cycle. The southern-most groundtrack clips the northern edge of Monterey Bay, the second intersects the coast at Point Arena, the third between Cape Blanco and Cape Mendicino, and the northern-most in central Oregon.

The wavenumber power spectra on the southernmost groundtrack (solid black line) stays fairly regular over the seasonal cycle, showing reduced energies in September/October and November/December. The next groundtrack to the north, the Point Arena groundtrack (green dashed line), has similar energies in the first four months of the year, then the power increases in May/June. This energy persists through the months of July/August and September/October before weakening in November/December. The third groundtrack to the north (and offshore, blue dash-dot line) shows the same development for January to June as the line to the south of it, but in July/August and September/October the energy increases further and expands to longer wavelength, before dying down in November/December. Lastly, the spectra on the northern-most groundtrack has minimum energy in May/June and peaks in September/October.

This development can be understood by comparing the locations of these ascending tracks with the maps of seasonal velocity variance in Figure 3.9. As the

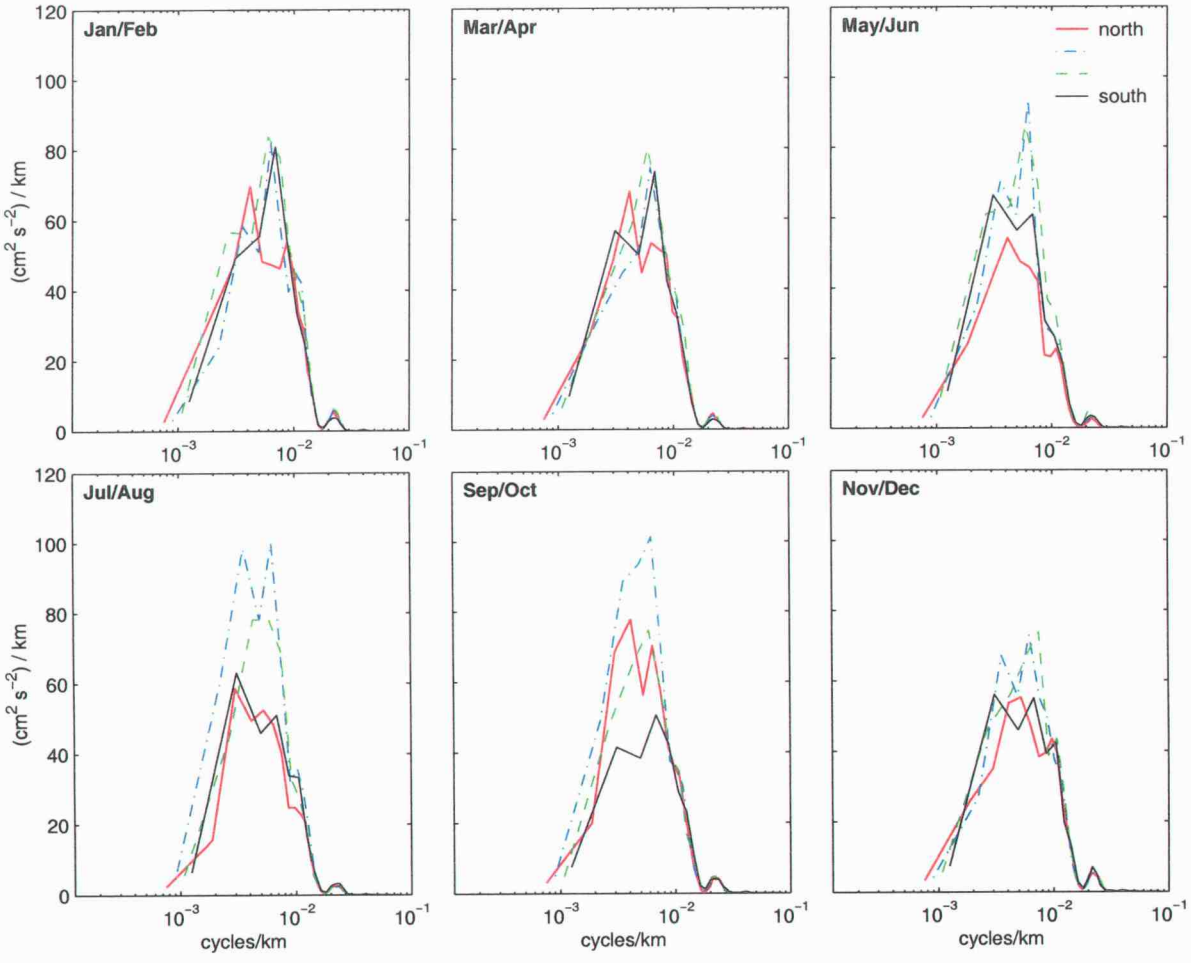

Figure 3.19: Wavenumber spectra from 1993 - 2000 for across-track geostrophic velocities on the four ascending tracks that intersect the coast between 35° and 45°N .

energy in the CC system begins to develop near the coast in spring, the wavenumber power spectra along the two central ascending tracks begins to increase. By July/August it has reached its maximum. In September/October, as the energy moves offshore past the Point Arena groundtrack (green dashed line), the power on that track begins to decrease. The November/December shows dissipated energy that shows up slightly at the northern-most line (black), and then more strongly in January/February.

Along the northern track these spectra generally show higher energy at longer wavelengths (250-300 km). Along the second most northern track, energy increases at these longer wavelengths in July-October. Along the most southern track, the shift to longer wavelengths occurs earlier (May/June, July/October), perhaps reflecting the earlier development of the summertime jet in the south.

4 DISCUSSION

4.1 Compare with previous work

Lynn and Simpson [1987], using 23 years of CalCOFI data, show a tongue of high standard deviation of dynamic height off of southern California and Baja. Their data shows a continuous band from 27°N that strengthens to the northern edge of their domain (at ~36°N). The gridded geostrophic velocity variance in 3.8 show a similar high variance in the California Bight, but it is not as strongly connected to the north. This could be due to the groundtrack spacing being too wide to see the connection.

The wavenumber spectra presented by *Strub and James* [2000] are based on four years of TOPEX altimeter data (October 1992 - October 1996). Our energy values are larger by a factor of ~2 in all cases. I believe this is due to multiplying here by 2 to present total variance in a single-sided PSD. Our results using eight years of data show similar results.

4.2 Offshore propagation

We compute the speed of the offshore propagation of the SSH signals in the Hovmöller diagrams by using a radon transform [*Deans*, 1983]. The radon transform is an image processing method that is used to objectively define linear

structures in images. In this case we use it to define the angle of the high and low SSH signals in the Hovmöller diagrams.

The radon transform is defined

$$\hat{g}(x',\theta) = \int_{-\infty}^{\infty}\int_{-\infty}^{\infty} g(x,y)\,\delta(x' - x\cos\theta - y\sin\theta)\,dx\,dy$$

where δ is the Dirac delta function. In essence, the image is rotated by θ and a line integral taken perpendicular to all points on the new x axis. This results in a transform dependent on θ and x', the distance along the rotated axes. By taking the sum of squares of the radon transform at each x' we can determine at what angle the maximum power of the transform occurs, which corresponds to the angle of the strongest linear structures in the image. Then using the time and distance increments of the Hovmöller image, the speed of the offshore movement of SSH signals is easily calculated. By applying this approach to the full Hovmöller diagrams we are taking an average over the eight years and the 1500 km offshore extent of the data presented.

We compare these offshore propagation speeds to Rossby wave phase speeds calculated from the Rossby radius of deformation dataset presented by *Chelton et al.* [1998]. They use climatological average temperature and salinity profiles to define the Rossby radius of deformation, L_R, on a 1° ×1° global grid. The theoretical Rossby wave phase speed [*Pedlosky*, 1979] is

$$c_0 = -\beta L_R^2$$

Figure 4.1 shows the comparison between our observations of offshore SSH

propagation speeds and the theoretical Rossby wave speeds using the *Chelton et al.* [1998] deformation radii, averaged over 5, 10 and 20° next to the coast. The observations are based on the radon transform of Hovmöller diagrams for 2° latitude bands from 24°N to 48°N . The *Chelton et al.* [1998] data are averaged over corresponding latitude bins with varying offshore extent. South of 35°N the observations correspond well with the calculated phase speeds within 5° of the coast. At 35°N the observations show a marked increase in propagation speed and northward of 35°N observed propagation speeds are faster than all of the theoretical phase speeds. Since 35°N defines the northern edge of the California Bight, the change in offshore propagation speeds possibly reflects the different dynamics of the Bight.

Since the SSH signal moving offshore in the Hovmöller diagrams is strongest in the coastal region we should expect the offshore propagation speeds to be more dependent on this area. This would suggest that the calculated phase speeds from points within 5° of the coast would result in the best agreement, but this turns out to be false. The observed speeds are a factor of 1.5-2 times greater than the calculated phase speeds.

4.3 Effects of El Niño

The effect of the 1997-1998 El Niño is seen most clearly in the SSH Hovmöller diagrams. In Figure 3.11 the El Niño shows up in the 35° - 41°N latitude band as

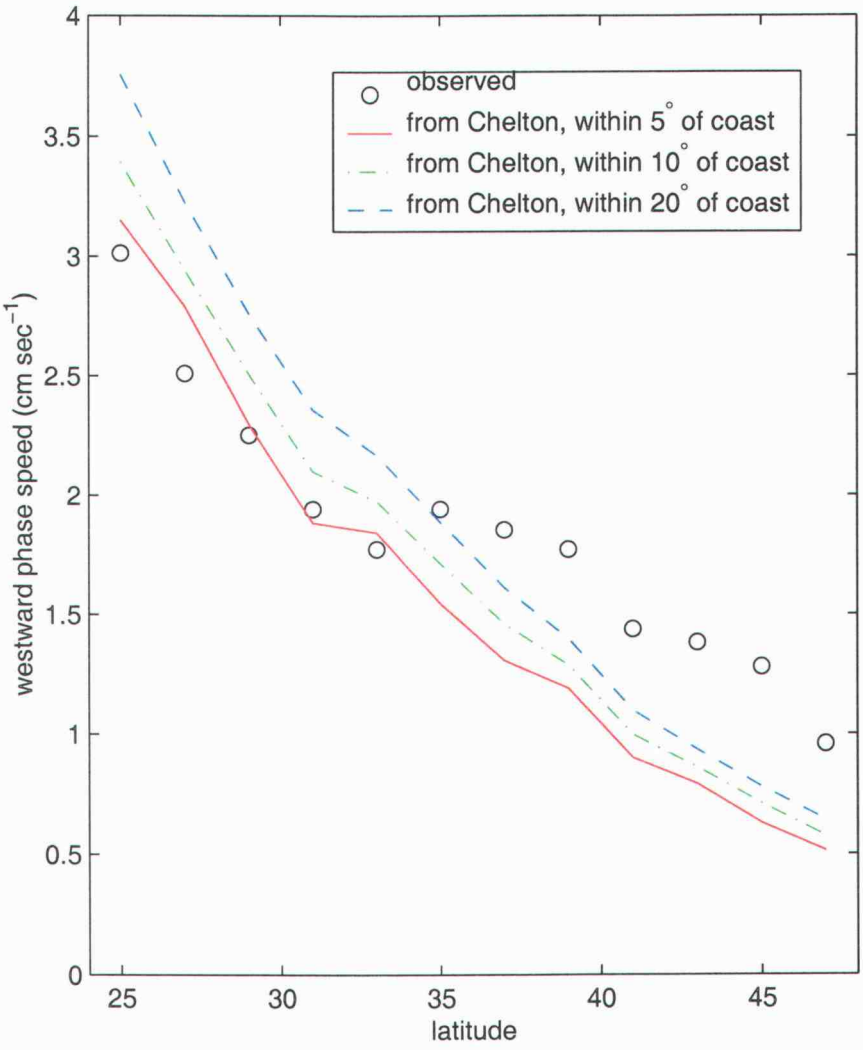

Figure 4.1: Offshore propagation speeds of TOPEX SSH signals as function of latitude from the Hovmöller diagrams (circles), compared to the Rossby wave phase speed calculated from the *Chelton et al.* [1998] Rossby radius atlas. The Rossby phase speeds are calculated using data within 5, 10 and 20 degrees of the coast (solid, dash-dot and dash lines, respectively).

high SSH anomaly values that begin in late 1997 near the coast. This high SSH propagates offshore like the typical seasonal height variations, but persists more strongly into the offshore domain. The following upwelling seasonal low shows up weakly and later in the season than in previous years. Farther north at 41° - 48°N (Figure 3.12) the El Niño signal shows up at the same time but doesn't suppress the following low SSH anomaly as strongly.

In the psuedo-EKE Hovmöller diagrams, the El Niño signal is also evident. At 35° - 41°N (Figure 3.13) the cross-track velocity energy in late 1997 and early 1998 is low just offshore of the coast. The California Current velocities develop later than previous years and are weaker. And as mentioned earlier, the following seasons show a less coherent development and offshore movement of the pEKE. It is not clear whether this is somehow an effect of the 1997-1998 El Niño.

The corresponding effect by the El Niño on wavenumber spectra is seen in the individual seasons presented in Figure 4.2. These plots are constructed with only data from the three months of each season and are therefore noisier than the 8 year means. The upper left panel shows the Fall 1997: the inshore line (red solid) shows similar wavenumber energy as seen in the 8 year mean (Figure 3.18), but the 400 km offshore groundtrack has reduced energy. Then in the upper right and lower left, the winter and spring of 1998 shows low values on all groundtracks. This is opposed to the 8 year mean results which show the inshore energy moving offshore and dissipating. In the El Niño year the the strong peak of energy in

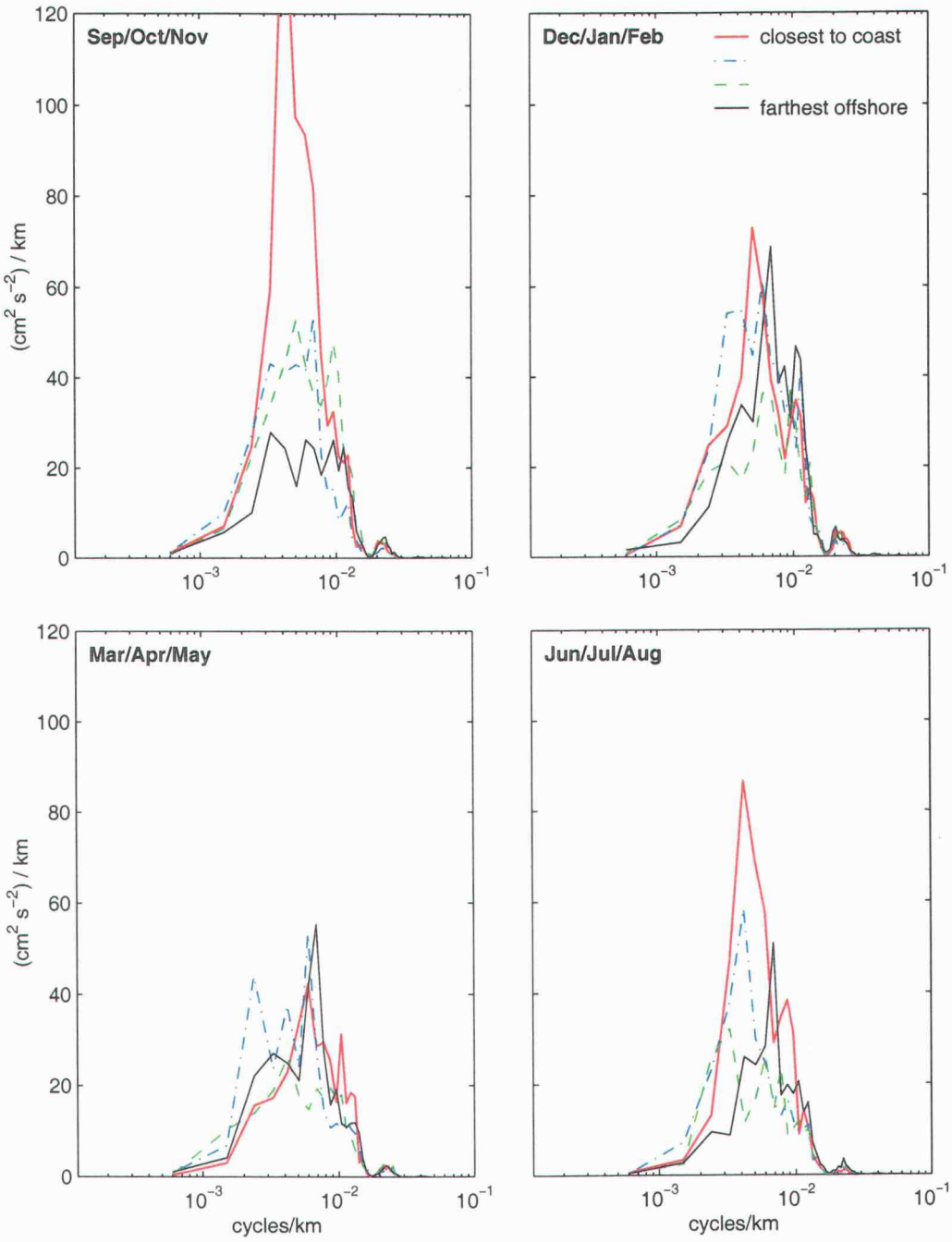

Figure 4.2: Wavenumber spectra from the 1997-98 El Niño period for across-track geostrophic velocities on the four descending tracks closest to the coast. Only groundtrack points between 30° and 50°N on each track are used.

Fall 1997 on the nearshore groundtrack is suppressed and doesn't show up at the offshore groundtracks in the following seasons. By the summer of 1998 the CC system is starting to develop (lower right panel) but has lower energy values than in the mean development.

4.4 Partitioning of the intraseasonal variance

We have presented the intraseasonal variance and shown how it is equal to the sum of the unnormalized within season and seasonal mean variances. To evaluate the contribution of each of these terms to the intraseasonal geostrophic velocity variance we show their ratio (Figure 4.3) and difference (Figure 4.4). In Figure 4.3 the seasonal mean variance divided by the within season variance is plotted with values ¿1 shown in red. In spring a blue band close to the California coast shows that the ratio is less than one, or that the within season variance is stronger. This band has expanded in summer, but is no longer coherent in fall. The areas where the seasonal mean variance is larger are patchy and scattered offshore in winter and spring. In summer there is a strong region of seasonal mean dominance offshore at -132°W, 39°N. Once again, the 1998 eddy can be seen moving to the southwest from fall through summer.

Figure 4.4 presents the difference between the seasonal mean and within season variances. Here the red sticks represent positive values, or points where the seasonal mean variance is larger. Comparison between this figure and the intraseasonal

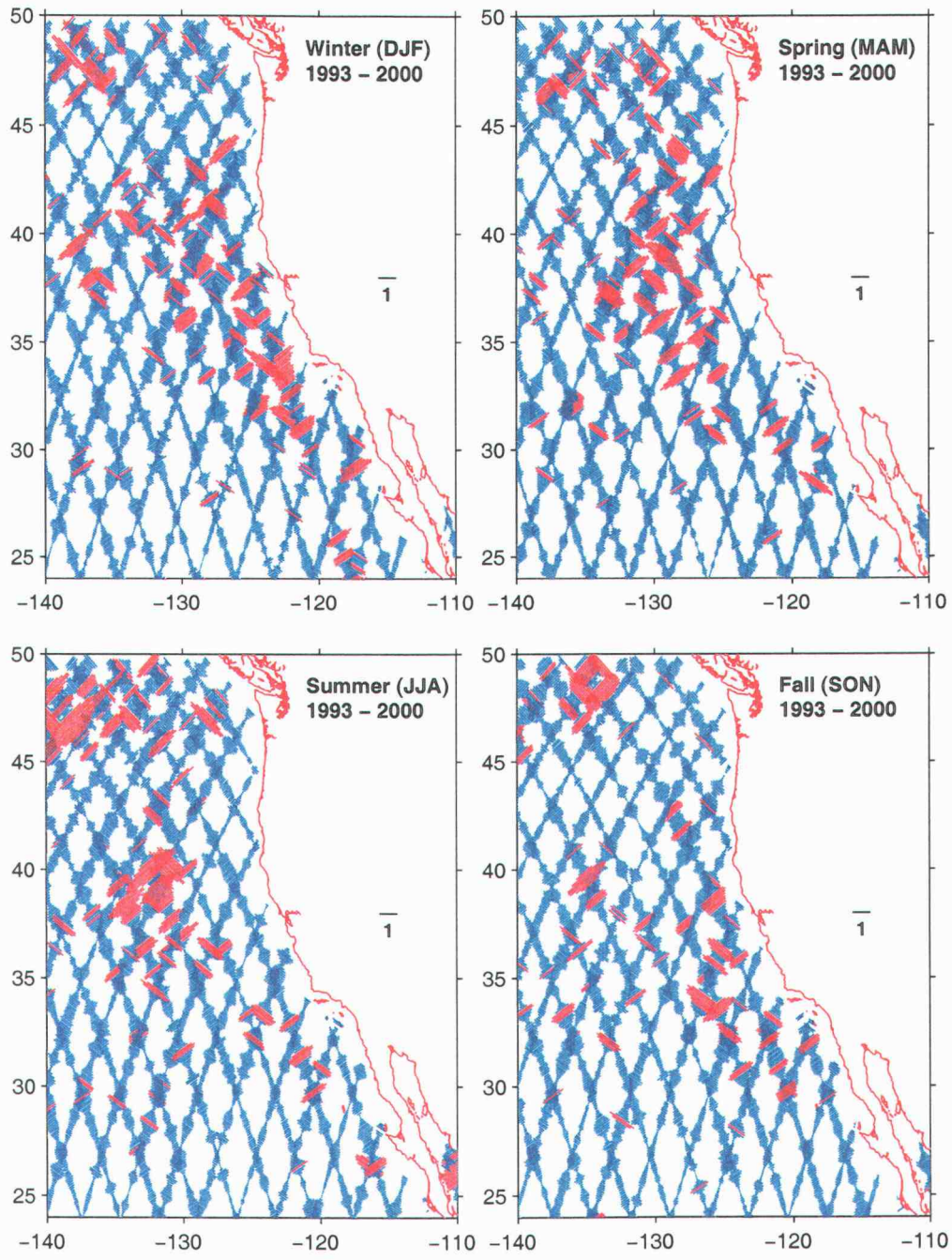

Figure 4.3: The ratio of the seasonal mean variance and the within season variance of geostrophic velocity from 1993-2000. Magnitudes greater than one (where the seasonal mean variance is larger) are plotted as red sticks.

variance (Figure 3.15) shows that in spring and summer the points where the within seasonal variance is dominant reflect the development of the intraseasonal variance: nearshore highs in spring expand into the energetic "C" in summer. This is generally holds true in fall also, but the seasonal mean variance show some strength offshore of southern California in the lower cusp of the "C". In winter the difference shows no coherent pattern, suggesting that the energies in the intraseasonal variances must be composed of equal parts within season and seasonal mean variance.

When the CC jet begins to develop in spring its location and time of development (at least within the 3 month seasonal windows we are using) do not have significant interannual variability. This continues to hold true in summer as the strength of the jet increases and it spreads to the offshore region. In fall when the CC shows signs of separation from the coast, the within season variance still dominates off Oregon and southwest of Cape Blanco. But because the location of the jet and its meanders and eddies is variable in the area south of Cape Blanco and offshore of central California, the seasonal mean variance gains strength. Winter sees the CC energy move offshore and weaken such that interannual differences show up in the seasonal mean variances.

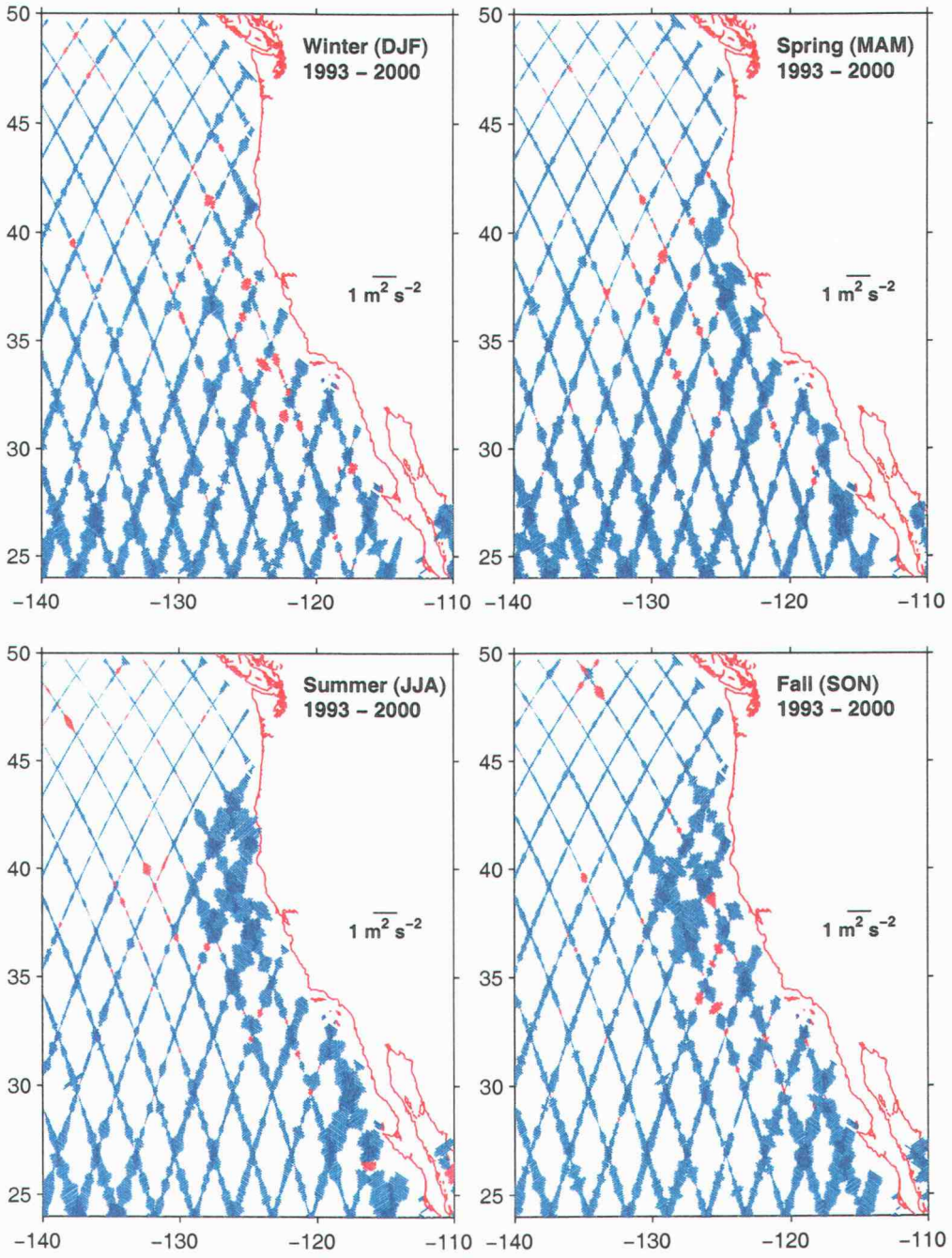

Figure 4.4: The seasonal mean variance minus the within season variance of geostrophic velocity from 1993-2000. Positive magnitudes (where the seasonal mean variance is larger) are plotted as red sticks.

5 CONCLUSION

The use of eight years of TOPEX data allows the seasonal development of variability in the California Current system to be well defined. The annual SSH and geostrophic velocity variances show an energetic C-shaped region from the coast at 45°N south to an offshore limit of ~135°W between 35° - 40°N and then back toward shore south of the California Bight at 30°N. The seasonal development of the CC shows SSH and velocity variances begin to increase near the coast in spring as equatorward currents appear. In summer the currents have moved offshore and maximum variances are seen ~300 km from the coast. In fall the energetic region has expanded and has spread westward and variance peaks of 500 cm^2s^{-2} are seen. Winter sees decreased but still significant variances in the offshore region as the CC surface jet weakens.

Along-track wavenumber power spectra are also used to describe the seasonal development and variability of the system. The wavenumber energy on tracks paralleling the coast (descending tracks) and intersecting the coast (ascending tracks) is described. As the CC system develops, wavenumber energy increases at 200-300 km wavelengths. This energy propagates offshore and weakens. At the offshore tracks the wavenumbers show weaker energies and shorter wavelengths (150-200 km),

Offshore propagation of SSH is shown to be strongly coherent in the Hovmöller diagrams presented. Positive SSH anomalies can be traced O(1000) km off the

coast. The dependence of the offshore phase speed is seen to agree with the theoretical Rossby wave speed south of 35°N but to be larger by a factor of 1.5-2 north of 35°N The Hovmöller diagrams for cross-track velocity energy show similar phase speeds, but the energy does note propagate as far into the ocean interior. In the 35° - 41°N latitude band the energy signal is seen only ~600 km offshore, while to the north at 41° - 48°N it is even less with a maximum of 300 km.

The partitioning of the intraseasonal variance between within season and seasonal mean variance is investigated. The within season variance is strongest in the region where the CC jet develops and strengthens offshore in spring and summer. In fall this still holds true in the upper half of the energetic "C" region, but in the southern part, offshore of Central California, the seasonal mean variance contributes significantly. The seasonal mean variance is also important in the variance signal of the 1998 eddy near the northern edge of the domain.

Lastly, the 1997-1998 El Niño is included in this dataset and it's affects on variability are discussed. The El Niño can be seen clearly in the SSH Hovmöller diagrams as anomalously high values that begin in late 1997 at 35° - 41°N and propagates strongly into the offshore domain. The following low SSH upwelling signal is suppressed and shows up later in the year than is typical. The power in the wavenumber spectra is reduced on the descending tracks closest to the coast in Fall 1997 and the offshore propagation of energy is not seen in the following winter and spring.

BIBLIOGRAPHY

Bratseth, A. M., Statistical interpolation by means of succesive corrections, *Tellus*, pp. 439–447, 1986.

Brink, K. H., R. C. Beardsley, P. P. Niiler, M. Abbott, A. Huyer, S. Ramp, T. Stanton, and D. Stuart, Statistical properties of the near-surface flow in the California coastal transition zone, *J. Geophys. Res.*, pp. 14,693–14,706, 1991.

Chelton, D. B., R. A. deSzoeke, M. G. Schlax, K. El Naggar, and N. Siwertz, Geographical variability of the first baroclinic Rossby radius of deformation, *J. Phys. Oceanogr.*, *28*, 433–460, 1998.

Chelton, D. B., J. C. Ries, B. J. Haines, L.-L. Fu, and P. S. Callahan, Satellite altimetry, in *Satellite Altimetry and the Earth Sciences: A Handbook for Techniques and Applications*, edited by L.-L. Fu and A. Cazenave, pp. 1–131, Academic Press, 2001.

Chereskin, T. K., M. Y. Morris, P. P. Niiler, P. M. Kosro, R. L. Smith, S. R. Ramp, and D. L. Musgrave, Spatial and temporal characteristics of the mesoscale circulation of the California Current from eddy-resolving moored and shipboard measurements, *J. Geophys. Res.*, *105*, 1245–1269, 2000.

Crawford, W. R., J. Y. Cherniawsky, and M. G. Foreman, Formation of the Haida - 1998 oceanic eddy, *J. Geophys. Res.*, 2001, submitted.

Deans, S. R., *The radon transform and some of its applications*, Wiley-Interscience, New York, 1983.

Kelly, K. A., R. C. Beardsley, R. Limeburner, K. H. Brink, J. D. Paduan, and T. K. Chereskin, Variability of the near-surface eddy kinetic energy in the California Current based on altimetric, drifter, and moored current data, *J. Geophys. Res.*, *103*, 13,067–13,083, 1998.

Levitus, S., and R. Gelfeld, NODC inventory of physical oceanographic profiles, in *Key to Oceanography Records Documentation, No. 18*, U.S. Gov. Printing Office, 1992.

Lynn, R. S., and J. J. Simpson, The California Current system: The seasonal variability of its physical characteristics, *J. Geophys. Res.*, *92*, 12,947–12,966, 1987.

Marchesiello, P., J. C. McWilliams, and A. Shchepetkin, Equilibrium structure and dynamics of the California Current System, *J. Phys. Oceanogr.*, 2001, submitted.

Pedlosky, J., *Geophysical Fluid Dynamics*, Springer-Verlag, New York, 1979.

Schlax, M. G., and D. B. Chelton, Frequency domain diagnostics for linear smoothers, *J. Amer. Statistical Assoc.*, pp. 1070–1081, 1992.

Strub, P. T., and C. James, Altimeter-derived variability of surface velocities in the California Current System: 2. Seasonal circulation and eddy statistics, *Deep-Sea Res. II*, *47*, 831–870, 2000.

Swenson, M. S., and P. P. Niiler, Statistical analysis of the surface circulation of the California Current, *J. Geophys. Res.*, *101*, 22,631–22,645, 1996.